



**TOOLS**

# Tyramide signal amplification mass spectrometry (TSA-MS) ratio identifies nuclear speckle proteins

Joseph Dopie<sup>1</sup>, Michael J. Sweredoski<sup>2</sup> , Annie Moradian<sup>2</sup>, and Andrew S. Belmont<sup>1</sup> 

**We present a simple ratio method to infer protein composition within cellular structures using proximity labeling approaches but compensating for the diffusion of free radicals. We used tyramide signal amplification (TSA) and label-free mass spectrometry (MS) to compare proteins in nuclear speckles versus centromeres. Our “TSA-MS ratio” approach successfully identified known nuclear speckle proteins. For example, 96% and 67% of proteins in the top 30 and 100 sorted proteins, respectively, are known nuclear speckle proteins, including proteins that we validated here as enriched in nuclear speckles. We show that MFAP1, among the top 20 in our list, forms droplets under certain circumstances and that MFAP1 expression levels modulate the size, stability, and dynamics of nuclear speckles. Localization of MFAP1 and its binding partner, PRPF38A, in droplet-like nuclear bodies precedes formation of nuclear speckles during telophase. Our results update older proteomic studies of nuclear speckles and should provide a useful reference dataset to guide future experimental dissection of nuclear speckle structure and function.**

## Introduction

While different cellular compartments and structures have distinct protein compositions, methods for easily analyzing the protein composition of these different compartments and how they vary with changes in cell differentiation or physiology are limited (Bell et al., 2001; Croze and Morr , 1984; Mootha et al., 2003; Taylor et al., 2003). Biochemical purification is frequently accompanied by loss of specific proteins. Moreover, cellular bodies and structures that are not surrounded by lipid membranes may lose their physical integrity during biochemical isolation. Bodies with liquid-like properties are particularly prone to such disruptions with physical isolation procedures. For example, previous biochemical purification of interchromatin granule clusters (IGCs), also known as nuclear speckles, has enriched for individual granules present within IGCs; the extent to which nongranule components of the IGCs are lost during purification is unknown (Mintz et al., 1999; Saitoh et al., 2004).

Enzyme-based proximity labeling methods for tagging and then purifying the tagged proteins within particular cellular structures have been developed as an alternative to biochemical purification. Proximity labeling methods work to label proteins in situ with the goal of preserving cell structure during labeling. Thus, proximity labeling approaches are particularly well suited for enriching proteins within less stable and hard-to-purify

cellular structures. For example, proximity-dependent biotin identification uses in vivo expression of a biotin ligase, targeted to a specific cell structure, to biotinylate proteins in the vicinity of the targeted biotin ligase. The biotin ligase (BirA) is engineered (BirA\*) to label proteins “promiscuously,” with current models suggesting the release of a biotinoyl-5'-AMP that diffuses to label nearby proteins (Roux et al., 2012). Engineered ascorbate peroxidase (APEX) also uses in vivo expression of a cytoplasmic peroxidase to generate short-lived biotin-phenoxy radical, from biotin-phenol, that diffuses to label tyrosines on nearby proteins. Again, targeting the APEX enzyme to specific cell structures enables labeling of nearby proteins (Rhee et al., 2013).

A major unknown for all enzyme-based proximity labeling approaches is how far the labeling can spread from the targeted enzyme generating the label. Current estimates point to a radius of ~10 nm for biotin identification, which may be too small for complete labeling coverage of cellular organelles and bodies (Kim et al., 2014). The literature has cited an APEX staining radius of ~20 nm, based on the visualization by electron microscopy of a polymerized DAB product catalyzed by free radicals produced by APEX (Martell et al., 2012). However, this reported staining radius is an underestimation as it does not take into consideration that the DAB product visualized by electron

<sup>1</sup>Department of Cell and Developmental Biology, University of Illinois at Urbana-Champaign, Urbana, IL; <sup>2</sup>Proteome Exploration Laboratory, Department of Biology and Biological Engineering, Beckman Institute, California Institute of Technology, Pasadena, CA.

Correspondence to Andrew S. Belmont: [asbel@illinois.edu](mailto:asbel@illinois.edu).

  2020 Dopie et al. This article is distributed under the terms of an Attribution–Noncommercial–Share Alike–No Mirror Sites license for the first six months after the publication date (see <http://www.rupress.org/terms/>). After six months it is available under a Creative Commons License (Attribution–Noncommercial–Share Alike 4.0 International license, as described at <https://creativecommons.org/licenses/by-nc-sa/4.0/>).

microscopy is a precipitant deposited near the site of the peroxidase.

Tyramide signal amplification (TSA), an older method that preceded APEX, uses exogenous HRP targeted by immunostaining to generate tyramide (phenoxy) radicals (Bobrow et al., 1989, 1991; van Gijlswijk et al., 1996, 1997). HRP is more active than APEX and has been used to label proteins in extracellular, oxidizing compartments (Loh et al., 2016; Martell et al., 2016) and fixed samples (Bar et al., 2018). In fact, the staining radius of the HRP-generated radical, whose concentration decays exponentially from the HRP source, has been estimated by light microscopy at  $\sim 0.5\text{--}1\ \mu\text{m}$  (Carter et al., 2002; Chen et al., 2018). While the staining radius of the phenoxy radical generated by APEX in the living cell has not been likewise measured, it is likely similar. The estimated staining radius of TSA, and possibly APEX, may exceed the size of some targeted cell structures.

Here, we describe our application of TSA to the proximity labeling and proteomic analysis of IGCs/nuclear speckles. Nuclear speckles are irregularly shaped nuclear bodies that vary in size and number depending on the cell type (Galganski et al., 2017) and are thought to form by protein–protein and protein–RNA interactions (Shevtsov and Dundr, 2011). Previously, nuclear speckle protein composition was characterized biochemically, through isolation of the individual granules contained within IGCs. Over 80% of the proteins identified in this granule fraction were proteins involved in RNA synthesis and processing (Saitoh et al., 2004).

We describe a simple but key approach whereby we compare the relative abundances of proteins identified by TSA labeling of nuclear speckles versus centromeres. The nuclear speckle enrichment of each protein was determined based on its relative abundance in the pull-down fractions from nuclear speckles versus centromeres after TSA labeling. This approach minimized nonspecific background and false-positive hits (Mellacheruvu et al., 2013), producing a list of several hundred proteins as enriched in nuclear speckles. The majority of these proteins are associated with RNA synthesis and/or processing and overlapped ( $\sim 60\%$ ) with the proteins identified in the previous proteomic analysis of isolated IGC granules. Approximately two thirds of the top 100 sorted proteins have been shown previously by light microscopy to accumulate in nuclear speckles.

In addition, we validated by light microscopy the nuclear speckle localization of several proteins, including the pre-mRNA processing factor microfibrillar-associated protein 1 (MFAP1; Andersen and Tapon, 2008; Bertram et al., 2017). Interestingly, MFAP1 levels modulate the size of nuclear speckles and may contribute to the nucleation of nuclear speckles after mitosis.

## Results

### Experimental goals and design of the staining approach

We applied TSA (Bobrow et al., 1989; Wang et al., 1999; Fig. 1 A and Fig. S1 A) proximity labeling of proteins followed by comparative MS (mass spectrometry) of multiple cellular compartments, a simple, robust, cost effective, and easily applicable approach that is suitable for some membrane-less nuclear bodies/compartments. Given that the estimated staining radius of

the TSA reaction is roughly comparable to the size of some nuclear bodies, we reasoned that proteins identified by TSA labeling would contain a significant fraction of nonspecific proteins. To overcome the possibility of enriching and identifying extraneous proteins outside the structure of interest, we compared the abundance of proteins in a “target” nuclear body/structure to a “reference” body and tested our approach using nuclear speckles and centromeres as target and reference bodies, respectively (Fig. 1, A and B).

Nuclear speckles, ranging from  $\sim 0.4$  to  $2\ \mu\text{m}$  in diameter (Fakan and Puvion, 1980), are typically depleted from the nuclear periphery, enriched in the nuclear interior (Carter et al., 1991), and surrounded by the A1 Hi-C active chromosomal sub-compartment (Chen et al., 2018). Centromeres and their flanking pericentric heterochromatin, on the other hand, are heterochromatic, with a protein composition distinct from the active chromatin regions surrounding nuclear speckles (Fodor et al., 2010; Müller-Ott et al., 2014; Obuse et al., 2004). Centromeres are present throughout the nucleus but nonrandomly associate with the nuclear periphery and nucleolus (Carvalho et al., 2001). Therefore, we reasoned that centromeres would be good reference nuclear body for comparison with nuclear speckles. Moreover, both centromeres (Obuse et al., 2004) and nuclear speckles (Mintz et al., 1999; Saitoh et al., 2004) have been targets of previous proteomic analysis, and many proteins have already been validated by microscopy as enriched in either centromeres or nuclear speckles.

We determined TSA-labeling conditions producing specific staining of nuclear speckles and centromeres in human U2OS cells (Fig. 1 B). For the TSA reaction, we modified conditions developed earlier for TSA sequencing (Chen et al., 2018). Cells were grown to  $\sim 90\%$  confluency, fixed with PFA, and stained first with primary antibodies against either SC35 or CENPA followed by HRP-conjugated secondary antibodies. Next, we incubated cells with TSA reaction buffer containing tyramide and  $\text{H}_2\text{O}_2$  in PBS. For one replicate, we added sucrose to the TSA reaction buffer, which slightly reduces the TSA staining radius (Chen et al., 2018). Initially, we used tyramide conjugated to biotin for avidin-biotin pull-down. However, Western blotting showed prominent background bands, likely produced by endogenous biotinylated proteins. Thus, we replaced biotin-tyramide with FITC tyramide (Fig. S1, A and B). To further reduce nonspecific background, we selected antibodies such that the same secondary antibody is used for both the target and reference structures.

### Protein pull-down and MS

We suspended TSA-labeled cells in lysis buffer supplemented with protease inhibitors and DNase I. Cell clumps were disrupted by passage through a 25G needle, and the cell suspension was sonicated to obtain a clear lysate. The lysate was centrifuged to remove cellular debris and FITC proteins were pulled down using agarose beads conjugated with anti-FITC antibodies. Proteins were eluted off the beads and resolved on polyacrylamide gel (Fig. 1 C and Fig. S1 C).

To test the TSA labeling and enrichment of labeled proteins, we examined Western blots probed with antibodies against FITC (Fig. S1 D) or SON and heterochromatin protein I  $\alpha$  (HP1 $\alpha$ ). SON and HP1 $\alpha$  are highly enriched in nuclear speckles and

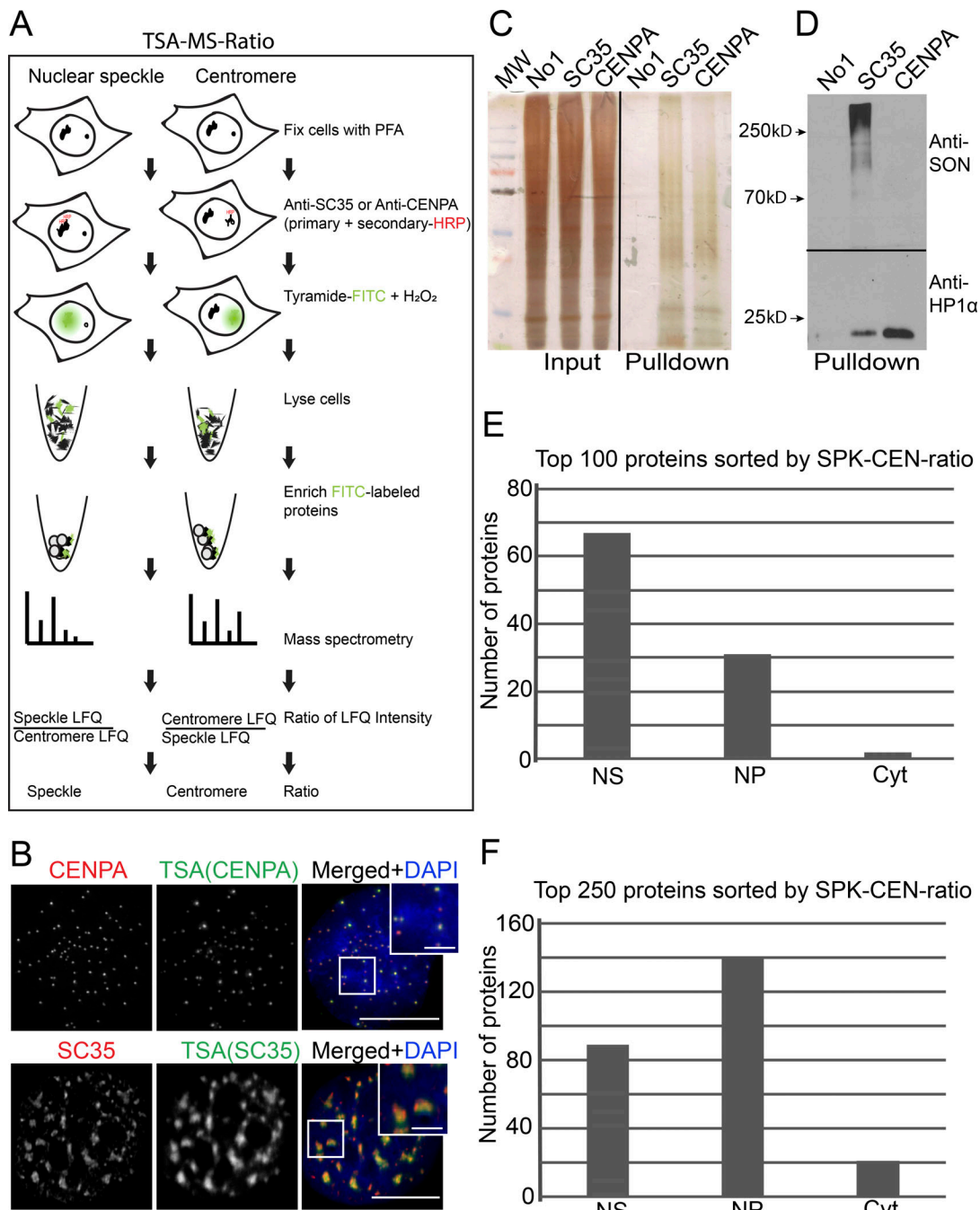


**Figure 1. TSA-MS ratio. (A)** Nuclear speckles or centromeres TSA-MS workflow. Nuclear speckles or centromeres were labeled using TSA with tyramide coupled to FITC (FITC-tyramide). FITC-labeled proteins were affinity purified and identified using tandem MS. The abundance of each protein in nuclear speckles or centromeres was estimated using LFQ, and the nuclear speckle versus centromere LFQ ratio for each protein was determined. **(B)** U2OS cell showing centromeres or nuclear speckles after combined immunofluorescence and TSA labeling, as indicated, and DNA (blue, DAPI) staining. Boxed areas are insets shown magnified. Scale bars: main panel, 5  $\mu$ m; inset, 2  $\mu$ m. **(C)** Silver-stained gels after TSA labeling (Input) and affinity pull-down of FITC-labeled proteins (Pull-down) from nuclear speckles or centromeres. Primary antibodies, including no primary antibody (No1), for TSA labeling are indicated at top of gel. **(D)** Western blot comparing SON and HP1 $\alpha$  levels in the nuclear speckle and centromere fractions after pull-down of FITC-labeled proteins, as in C. **(E and F)** Numbers of the top 100 (E) and top 250 proteins (F), sorted by their nuclear speckle versus centromere (SPK-CEN) ratios, located in nuclear speckles (NS), nucleoplasm (NP), or cytosol (Cyt). See also Table S1.

centromeres, respectively. Indeed, the nuclear speckle fraction was highly enriched with SON and depleted of HP1 $\alpha$ , whereas the centromere fraction was enriched with HP1 $\alpha$  and depleted of SON (Fig. 1 D).

Next, we repeated the TSA labeling and affinity pull-down but followed this by MS. The relative abundance of each protein in each of the two nuclear bodies was determined using label-free quantitation (LFQ; Cox et al., 2014).

There was an overlap of 1,620–1,870 identified proteins between paired-replicate nuclear speckle (SC35) TSA-MS experiments (Table S1) and 2,340–2,495 identified proteins between paired-replicate centromere (CENPA) TSA-MS experiments, with extensive overlap (60–90%) in the identified proteins from the combined nuclear speckle and centromere paired datasets (Table S1). We expected this extensive overlap between centromere and nuclear speckle identified proteins because of the large TSA-staining radius. Many overlapping proteins would be expected to be present in the nucleoplasm surrounding both nuclear bodies. Moreover, coimmunostaining revealed that centromeres and nuclear speckles, while typically spatially separated, occasionally localized close enough to each other so that their surrounding TSA-stained volumes would overlap. Additionally, we expected some proteins would be labeled due to the low-level nucleoplasmic distribution of CENPA and SC35 proteins outside of centromeres and nuclear speckles, respectively, as well as non-specific background primary and/or secondary antibody staining.

To identify candidate nuclear speckle proteins, we calculated the nuclear speckle versus centromere LFQ intensity ratio for each protein in each paired dataset (Table S1 and Fig. S2 A). The geometric mean of these ratios from replicate datasets was then taken as the nuclear speckle versus centromere (SPK-CEN) ratio. Only proteins quantified in both the nuclear speckle and paired centromere pull-down fractions were analyzed. We note that unique proteins that were quantified in the nuclear speckle, but not the paired centromere, fractions, including some known nuclear speckle proteins, were excluded (Table S1).

### High percentage of known nuclear speckle proteins among the top sorted proteins in TSA-MS ratio lists

Our knowledge of nuclear speckle proteins comes from three main sources. First is the cumulative literature describing microscopy localization of specific proteins to nuclear speckles. Second is the previous MS of biochemically fractionated IGC granules (Mintz et al., 1999; Saitoh et al., 2004). This work identified 146 proteins, including three proteins (SON, BCLAF1, and acinus) whose localization previously had been unknown but that were then validated as enriched in nuclear speckles using light microscopy (Saitoh et al., 2004; Table 1). Third is the Human Protein Atlas (HPA) survey of the staining patterns of thousands of different antibodies (Thul et al., 2017), which included a “localized to the nuclear speckles” annotation. Note that this assignment is based solely on the characteristic staining pattern observed and not on the actual colocalization of this staining pattern with a known nuclear speckle marker.

Our analysis also identified proteins previously shown by light microscopy to be enriched in nuclear speckles. Indeed, the list of proteins with the highest SPK-CEN ratios showed a very high percentage of these “validated” nuclear speckle proteins, with this percentage dropping with decreasing SPK-CEN ratio.

Specifically, 96% of the top 30 sorted proteins are validated as nuclear speckle proteins, including two proteins that we validated as localized to nuclear speckles (Table 1). This percentage, however, drops to 68% for the top 100 sorted proteins and 35% for the top 250 proteins (Fig. 1, E and F; Table 1; and Table S1). Roughly one third (23) of these 68 validated nuclear speckle

proteins in the top 100 sorted list, including PRPF4B, LUC7L3, and CDK12, had not been identified previously in the MS analysis of isolated IGC granules (Saitoh et al., 2004; Table 1 and Table S1).

Empirically, the SPK-CEN ratio cutoff corresponding to a nuclear speckle enrichment sufficient for wide-field light microscopy detection was  $\sim 1.65$  (ratio for 91th protein), with approximately three fourths of the top-sorted 91 proteins previously identified by light microscopy as nuclear speckle localized. This includes 7 out of the 10 proteins whose SPK-CEN ratio is equal to or just above this 1.65 ratio cutoff, as compared with 2 of the next 10 proteins whose ratio is just below this 1.65 cutoff. The actual level of enrichment in nuclear speckles is likely several-fold higher. Given the known radius of diffusion of the tryamide free radical, the actual volume of the tryamide-stained regions surrounding the centromeres and nuclear speckles should be several-fold larger than the volumes of the speckles or centromere regions themselves. Experimentally, SON, with the highest SPK-CEN ratio of 4.9, appears  $>10$ -fold enriched in nuclear speckles by wide-field deconvolution light microscopy and even more highly enriched in speckles as observed by super-resolution light microscopy (Chen et al., 2018; Kim et al., 2019).

Interestingly, the HPA annotates some previously validated nuclear speckle proteins as “mainly localized to the nucleoplasm” (Table 1), including ACINI1 (Saitoh et al., 2004) and SRSF2 (SC35; Fu and Maniatis, 1992), which currently is the most widely used nuclear speckle marker. Using light microscopy, we show in a later Results section (Validating potential nuclear speckle proteins) that three (MFAP1, pre-mRNA processing factor 38A [PRPF38A], and zinc finger 207 [ZNF207]) out of three proteins tested from the top 30 list, whose nuclear speckle localization had been unknown or ambiguous, were indeed nuclear speckle enriched. Thus, the true percentage of speckle-enriched proteins in our top-sorted lists may be significantly higher than the percentage of previously validated nuclear speckle proteins.

### Annotated functions of top sorted proteins in nuclear speckle-enriched TSA-MS ratio list

Similar to the findings from the previously published MS study of isolated IGC granules (Saitoh et al., 2004), a large fraction of proteins with high SPK-CEN ratio are also implicated in some aspect of RNA metabolism (Fig. S1, B and C; Table 1; and Table S1). Specifically, all of the top 30 sorted proteins (Table 1) are implicated in some aspect of RNA metabolism, including pre-mRNA splicing (25), poly(A) tail length control and RNA export (3), and transcription (2). Similarly, 90 of the top 100 proteins are functionally annotated as RNA processing or proteins engaged in transcription or transcription regulation (Fig. S2 C and Table S1). Moving further down the list, 186 of the top 250 proteins are involved in RNA metabolism, including pre-mRNA splicing factors (108), transcription (42), cleavage, polyadenylation or mRNA export (17), and other proteins annotated only as RNA-binding (19; Fig. S2 B and Table S1).

Structurally, nuclear speckles behave as liquid-droplet type bodies (Marzahn et al., 2016) and are thought to form through multivalent interactions between low-complexity domains (LCD) on multiple proteins as well as RNA-protein interactions. Most of the proteins with higher SPK-CEN ratio contain RNA-binding domains and/or LCDs (Table 1 and Table S1). One such

Table 1. List of the top 52 proteins sorted by SPK-CEN ratio

#	Gene name	Entry ID	SPK-CEN ratio	Protein domains	GO annotated process	Localization (IF)	IF references
1	SON	P18583	4.918	LCD, DRBM, G patch	Splicing	NS	HPA, Saitoh et al. (2004)
2	SRRM2	Q9UQ35	4.642	LCD, coiled coil	Splicing	NS	HPA, Mintz et al. (1999)
3	PRPF40A	O75400	3.050	LCD, coiled coil, WW	Splicing	NS	HPA
4	RBM25	P49756	2.722	LCD, RRM, coiled coil, PWI	Splicing	NS	HPA, Zhou et al. (2008)
5	ZNF207	O43670	2.564	LCD, ZnF	Transcription	NS	Rai et al. (2018), this study
6	LUC7L2	Q9Y383	2.413	LCD, coiled coil	Splicing	NS	Howell et al. (2007)
7	SRRM1	Q8IYB3	2.409	LCD, PWI	Splicing	NS	HPA
8	WTAP	Q15007	2.373	LCD, coiled coil	Splicing	NS	HPA, Little et al. (2000)
9	ZC3H14	Q6PJT7	2.362	LCD, ZnF	Poly(A) binding	NS	HPA, Leung et al. (2009)
10	ACIN1	Q9UKV3	2.341	LCD, coiled coil, RRM, SAP	Splicing	NS	Saitoh et al. (2004)
11	SAP18	O00422	2.328	LCD	Splicing	NS	Singh et al. (2010)
12	DDX46	Q7L014	2.299	LCD, DEXD, HELICc	Splicing	NS	HPA, Will et al. (2002)
13	TRA2A	Q13595	2.295	LCD, RRM	Splicing	NS	Platt et al. (2015)
14	SRSF2	Q01130	2.284	LCD, RRM	Splicing	NS	Fu and Maniatis (1990)
15	DDX23	Q9BUQ8	2.263	LCD, coiled coil, DEXDc, HELICc	Splicing	NP	HPA
16	CDK12	Q9NYV4	2.247	LCD, S_TKc	Transcription	NS	Ko et al. (2001)
17	PRPF4B	Q13523	2.239	LCD, coiled coil	Splicing	NS	HPA
18	LUC7L3	O95232	2.238	LCD, coiled coil	Splicing	NS	HPA, Umehara et al. (2003)
19	MFAP1	P55081	2.230	LCD, coiled coil	Splicing	NS	This study, Salas-Armenteros et al. (2019)
20	SF3A1	Q07955	2.227	LCD, RRM	Splicing	NS	HPA, Huang et al. (2011)
21	SF3B2	Q13435	2.205	LCD, coiled coil	Splicing	NS	HPA, Terada and Yasuda (2006)
22	RBM39	Q14498	2.200	LCD, RRM	Splicing	NS	HPA, Imai et al. (1993)
23	RBM10	P98175	2.181	LCD, RRM, ZnF, G patch	Splicing	NS	HPA, Inoue et al. (2008)
24	SRSF1	Q07955	2.137	LCD, RRM	Splicing	NS	Cáceres et al. (1997)
25	RBM26	Q5T8P6	2.123	LCD, ZnF, RRM, coiled coil	RNA binding	NS	HPA
26	SF3A3	Q12874	2.077	LCD, ZnF, coiled coil	Splicing	NS	Chiara et al. (1994)
27	RBM8A	Q9Y5S9	2.074	LCD, RRM	Splicing	NS	HPA
28	RBM27	Q9P2N5	2.062	LCD, RRM	RNA binding	NS	HPA
29	PRPF38A	Q8NAV1	2.048	LCD, coiled coil	Splicing	NS	This study
30	SNRPA1	P09661	2.038	LCD, LRRcap	Splicing	NS	HPA
31	PUF60	Q9UHX1	2.030	LCD, RRM	Splicing	NP	HPA
32	SAP30BP	Q9UHR5	1.998	LCD	Transcription	NP	Li et al. (2004)
33	PRPF6	O94906	1.996	LCD, coiled coil, HAT	Splicing	NS	HPA
34	RNPS1	Q15287	1.993	LCD, RRM	Splicing	NS	Trembley et al. (2005)
35	AURKA	O14965	1.982	S_TKc	Kinase	NP	HPA
36	RBM17	Q96I25	1.979	LCD, G patch, RRM	Splicing	NP	HPA
37	LSM3	P57743	1.948	Sm	Splicing	NP	HPA
38	SF3B1	O75533	1.946	LCD, coiled coil	Splicing	NS	HPA
39	RPRD1B	Q9NQG5	1.942	RPR, coiled coil	Transcription	NP	HPA
40	CAPRIN1	Q14444	1.931	LCD, coiled coil	RNA-binding	Cy	Solomon et al. (2007)
41	PRPF4	O43172	1.931	LCD, SFM, WD40	Splicing	NS	HPA
42	CDC5L	Q99459	1.915	LCD, SANT, coiled coil	Splicing	NS	Burns et al. (1999)

Table 1. List of the top 52 proteins sorted by SPK-CEN ratio (Continued)

#	Gene name	Entry ID	SPK-CEN ratio	Protein domains	GO annotated process	Localization (IF)	IF references
43	SRSF7	Q16629	1.909	LCD	Splicing	NP	HPA
44	PRPF8	Q6P2Q9	1.906	LCD, RRM, ZnF	Splicing	NS	<a href="#">Malinová et al. (2017)</a>
45	SNW1	Q13573	1.906	LCD	Splicing	NP	HPA, <a href="#">Zhang et al. (2003)</a>
46	DHX15	O43143	1.886	LCD, DEXDc, HELICc	Splicing	NS	HPA
47	XAB2	Q9HCS7	1.882	LCD, HAT	Splicing	NP	HPA, <a href="#">Onyango et al. (2016)</a>
48	TLE3	Q04726	1.877	LCD, WD40, coiled coil	Transcription	NP	HPA
49	KIAA1429	Q69YN4	1.876	LCD	Splicing	NS	<a href="#">Horiuchi et al. (2013)</a>
50	CHERP	Q8IWX8	1.867	LCD, G_patch, SWAP	Splicing	NS	<a href="#">Sasaki-Osugi et al. (2013)</a>
51	SART1	O43290	1.865	LCD, coiled coil	Splicing	NS	HPA
52	PSME3	P61289	1.859		Misc.	NS	<a href="#">Baldin et al. (2008)</a>

Also displayed are the annotated protein domains, GO Modular Architecture Research Tool SMART, HPA, the UniProt knowledgebase (<https://www.uniprot.org/>), as well as available literature. IF (immunofluorescence or fluorescent protein signal); FDEXD (DEXD/H-box helicase domain); DEXDc (DEAD-like helicases superfamily); HELICc (helicase superfamily c-terminal domain); HAT (Half-A-TPR repeats); DRBM (double-stranded RNA-binding motif); LRRcap (LRR-containing proteins); ZnF (zinc finger); S\_TKc (Serine/Threonine protein kinases, catalytic domain). NP, nucleoplasm; NS, nuclear speckle,

highly disordered protein, ZNF207/BuGZ, has been previously demonstrated to undergo phase transition to form liquid droplets as part of the mitotic spindle apparatus ([Jiang et al., 2015](#)).

#### Sorting proteins enriched in centromeres

Sorting proteins instead by the magnitude of the centromere versus nuclear speckle (CEN-SPK) ratio creates a list of potential centromere-enriched proteins, analogous to the previously defined nuclear speckle-enriched list ([Fig. 1 A](#)). However, in contrast to the significant enrichment of known nuclear speckle proteins among proteins with high SPK-CEN ratio, our list of proteins with high CEN-SPK ratio was dominated by proteins that localized to the nucleolus, nucleoplasm, or cytoplasm (Table S1). Of the top 100 proteins sorted by the CEN-SPK ratio, 50 are nucleolar proteins, while HPI $\alpha$  ([Kang et al., 2011](#)) and Aurora B kinase ([Yamagishi et al., 2010](#)) were the only well-characterized heterochromatin and/or centromere-associated proteins (Table S1).

This small number of validated centromere or heterochromatin proteins in our CEN-SPK ratio-sorted list does not appear to be a problem with the centromere TSA labeling and/or pull-down. Rather, many known centromere- and heterochromatin-associated proteins were present in the replicate centromere TSA-MS datasets but had no LFQ intensities in the paired nuclear speckle TSA-MS datasets (Table S1), including 10 CENP proteins (CENPC, CENPB, CENPH, CENPK, CENPT, CENPN, CENPI, CENPO, CENPP, and CENPX; [Obuse et al., 2004](#); [Verdaasdonk and Bloom, 2011](#)), HMG A2 ([Narita et al., 2006](#)), and HDAC1 ([Yamada et al., 2005](#); Table S1).

We chose centromeres as the reference nuclear body for our ratio approach, because we expected centromere labeling would include proteins present throughout the nucleoplasm, but not proteins enriched within or near nuclear speckles. Centromeres nonrandomly localize close to nucleoli and the nuclear periphery, which are regions not typically associated with nuclear

speckles. Moreover, centromeres are smaller than the diffusion radius of the tyramide radical, allowing significant labeling of the proteins in the surrounding nucleoplasm. Future application of the TSA-MS ratio to identify proteins specifically enriched in centromeres and other heterochromatin regions might benefit from a different reference target. Here, we focused our attention and further validation work on nuclear speckle-enriched proteins.

#### Validating potential nuclear speckle proteins

As described, many of the top sorted proteins in our SPK-CEN ratio list are previously validated nuclear speckle proteins (Table 1 and Table S1). However, the top-sorted lists also included proteins for which conflicting data previously existed with regard to their nuclear speckle localization, proteins previously identified as not enriched in speckles, or proteins with no information available regarding their possible nuclear speckle localization. Some proteins with high SPK-CEN ratio could be proteins specifically depleted from centromeres and the surrounding nucleoplasm rather than enriched within nuclear speckles (false positives). Other proteins with a high SPK-CEN ratio could be specifically enriched in nuclear speckles but have not been examined previously by microscopy or have incorrectly appeared not to be enriched in nuclear speckles due to some technical problem (false negatives).

Therefore, we investigated the nuclear speckle localization of 3 proteins among the top 30 sorted protein list: MFAP1, PRPF38A, and ZNF207. Both MFAP1 and PRPF38A are components of the spliceosome ([Agafonov et al., 2011](#); [Bertram et al., 2017](#)). They are implicated in pre-mRNA splicing ([Andersen and Tapon, 2008](#)) but are annotated as “localized to the nucleoplasm” by the HPA. ZNF207, also known as BUGZ, is a kinetochore and microtubule-binding protein ([Jiang et al., 2015](#)) recently shown to accumulate in nuclear speckles of preextracted

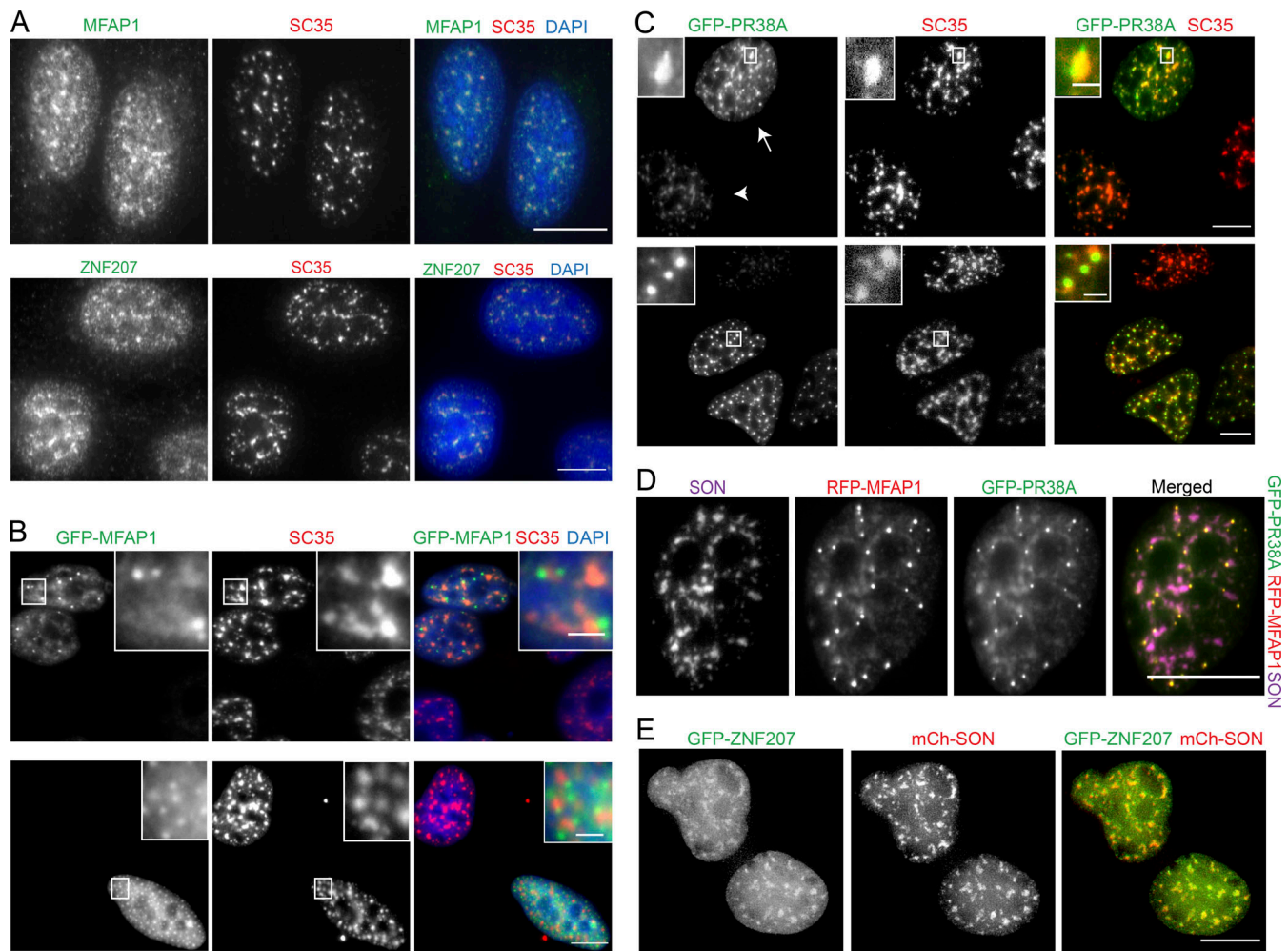


**Figure 2. Microscopy validation of proteins with a high SPK-CEN ratio.** (A) Nuclear speckle localization (SC35, red) of MFAP1 or ZNF207 (green) in U2OS after immunostaining of methanol-fixed cells (but not after formaldehyde fixation; see Fig. S2 D). DNA (DAPI), blue. (B and C) Nuclear speckle (SC35 immunostaining, red) localization of GFP-MFAP1 and GFP-PRPF38A (GFP-PR38A) after formaldehyde fixation at lower transgene expression levels (upper panel). At higher expression levels (lower panel), GFP-MFAP1 and GFP-PR38A increasingly form droplet-like bodies outside but frequently adjacent to nuclear speckles. (C) Arrowhead points to nucleus with lower GFP-PR38A expression and only nuclear speckle staining; arrow points to nucleus with high GFP-PR38A expression. Insets are magnifications of boxed areas. (D) Colocalization of tagRFP-MFAP1 (red) and GFP-PRPF38A (green) in nuclear speckles (SON immunostaining, magenta) and bodies outside of speckles in cells fixed with formaldehyde. (E) GFP-ZNF207 (green) localizes in nuclear speckles (Cherry-SON, red) in live cells (but not after formaldehyde fixation; see Fig. S2 E). Scale bars: main panel, 10  $\mu$ m; inset, 2  $\mu$ m.

cells (Rai et al., 2018) but annotated as “localized to the nucleoplasm” by the HPA.

Coimmunofluorescence staining using antibodies against MFAP1 or ZNF207 and antibody for SC35, to visualize nuclear speckles, showed nuclear speckle accumulation for both proteins in cells fixed with methanol (Fig. 2 A). Formaldehyde-fixed cells instead showed diffuse foci throughout the nucleoplasm (Fig. S2 D). However, recent reinvestigation of mitotic bookmarking revealed a large number of transcription factors that appear to lose their DNA binding during mitosis, as visualized after formaldehyde fixation, in fact show strong mitotic chromosome localization in live cells using fluorescently tagged protein expression. Live-cell imaging revealed a loss of transcription factor within seconds of adding formaldehyde (Teves et al., 2016).

To distinguish between these possibilities and to validate nuclear speckle localization of these proteins, we transfected

cells to express human MFAP1, PRPF38A, or ZNF207 proteins fused to GFP. GFP-MFAP1- or GFP-PRPF38A-expressing cells showed GFP accumulation in nuclear speckles after formaldehyde fixation (Fig. 2, B–D). Therefore, the apparent loss of nuclear speckle staining for these proteins likely reflects the sensitivity of their antibody epitopes to formaldehyde fixation. However, cells transiently transfected with GFP-ZNF207 and fixed with formaldehyde still showed diffuse nucleoplasm staining, similar to immunostaining of the endogenous ZNF207 protein (Fig. S2 E). Live-cell microscopy, however, showed GFP-ZNF207 colocalized with SON in nuclear speckles (Fig. 2 E).

This sensitivity of either antibody epitope preservation or protein nuclear speckle localization to formaldehyde fixation conditions (with or without preextraction) may account for previous negative or conflicting results for nuclear speckle localization for these three proteins. We note that while this

article was in preparation, MFAP1 was localized to nuclear speckles using the sequential combination of preextraction, formaldehyde fixation, and then ethanol fixation (Salas-Armenteros et al., 2019).

In addition to localizing within nuclear speckles, at high expression levels, both GFP-MFAP1 and GFP-PRPF38A also formed bright and distinct, intranuclear, round foci, which scored negative for both SC35 and SON nuclear speckle markers after immunostaining (Fig. 2, B–D). Some of these foci were adjacent to but distinct from nuclear speckles. Foci were absent in cells expressing lower levels of GFP-MFAP1 or GFP-PRPF38A (Fig. 2 C, arrowhead) but increased in number with increasing GFP-MFAP1 or GFP-PRPF38A expression (Fig. 2 C, arrow; Fig. 2 D), suggesting foci form as a result of overexpression.

Coexpression of MFAP1 and PRPF38A at higher expression levels revealed both proteins colocalized in nuclear speckles and the foci outside of and adjacent to nuclear speckles (Fig. 2 D).

### MFAP1 depletion increases nuclear speckle size

Proteins containing arginine/serine (RS) dinucleotide repeats, including members of the serine/arginine (SR) superfamily of pre-mRNA splicing factors, are typically enriched in nuclear speckles (Galganski et al., 2017) and comprise a large fraction of proteins with high SPK-CEN ratio (Table 1). SON, the protein with the highest SPK-CEN ratio (Table 1), is a very large, multidomain protein with a double-stranded RNA-binding domain, a RS repeat domain, and multiple tandem repeats; all of these domains could influence nuclear speckle composition and physical properties. Depleting SON changed nuclear speckle shape from a solid to doughnut shape and reduced the concentration of U1-70K snRNP and SF2/ASF proteins within nuclear speckles (Sharma et al., 2010).

We asked whether other proteins, especially non-SR proteins in the top 30 SPK-CEN ratio–sorted list, might also regulate nuclear speckle structure (Table 1). SRRM2, number 2 on this list, is also a large, SR-related protein that has many RS repeats (Wu and Maniatis, 1993) but lacks an RNA recognition motif (RRM) that is found in SR proteins (Long and Caceres, 2009), suggesting SRRM2 may interact with RNA in the presence of other SR proteins (Blencowe et al., 2000). SRRM2 knockdown (KD) by siRNA produced no observable change in nuclear speckle shape or size (Fig. S3, A and D). However, SRRM2 KD reduced the nuclear speckle association of SC35, but not SON, as visualized by immunostaining (Fig. S3 E), suggesting that SC35 also is not required for maintaining normal nuclear speckle size and shape.

ZNF207 undergoes phase transition to form liquid droplets that promote microtubule polymerization (Jiang et al., 2015). While ZNF207 has a high nuclear speckle enrichment (Rai et al., 2018; Fig. 2, A and E), it lacks both an RS domain and an RRM. Nuclear speckle morphology, and the nuclear speckle localization of SC35 and SON, were unchanged in ZNF207-depleted cells (Fig. S3, A and D).

In contrast, nuclear speckles became noticeably enlarged after MFAP1 KD (Fig. 3 B and Fig. S3 F). The average nuclear speckle in a typical MFAP1-depleted cell was  $\sim 3 \mu\text{m}$  along its widest length (maximum length,  $\sim 5 \mu\text{m}$ ), as compared with typical,  $\sim 0.5\text{--}2 \mu\text{m}$  lengths in control cells (Fig. S3 D; and Fig. 3,

B and C). MFAP1 depletion also increased nuclear speckle size in nontransformed human hTERT-immortalized Tig3 fibroblasts (Fig. S3, B and F) and CHO cells (Fig. S3, C and G). In CHO cells, MFAP1 depletion also increased SON nucleoplasmic levels (Fig. S3 G). We did not observe increased nuclear speckle roundness after MFAP1 KD (Fig. S3 D and Fig. 3 B).

Some nuclear speckles in MFAP1 KD cells migrated and encircled the periphery of nucleoli after RNA polymerase II (RNA pol II) transcription inhibition (Fig. 3, D–F; and Video 1). Longer exposure of MFAP1-depleted cells to  $\alpha$ -amanitin resulted in unusually large and fewer nuclear speckles per cell (five or fewer nuclear speckles in some cells), which sometimes surrounded remnants of nucleoli (Fig. 3 E). In contrast, KD of PRPF38A, which directly binds MFAP1 (Bertram et al., 2017; Ulrich et al., 2016), had no effect on nuclear speckle morphology (Fig. S3, A and D). These observations suggest that normal levels of MFAP1 are required to both maintain smaller nuclear speckle size and stabilize nuclear speckle interactions with other nuclear structures such as active chromatin.

### MFAP1 and PRPF38A partially separate from nuclear speckles into adjacent bodies after transcriptional inhibition

Overexpression of GFP-MFAP1 results in nuclear foci separate from and adjacent to nuclear speckles. In some GFP-MFAP1-overexpressing cells, nearly all GFP-MFAP1 is sequestered into the adjacent foci, with undetectable GFP-MFAP1 within the neighboring nuclear speckle (Fig. 2 B). RNA pol II transcription inhibition increases nuclear speckle size and roundness (Galganski et al., 2017). Furthermore, previous FRAP experiments showed that ASF/SF2 association with nuclear speckles depended on RNA pol II transcription (Kruhlak et al., 2000; Phair and Misteli, 2000). We therefore examined the association of GFP-MFAP1 to nuclear speckles after RNA pol II transcription inhibition.

As expected, inhibiting RNA pol II transcription caused nuclear speckles to become rounder but also caused fluorescently tagged MFAP1 and/or PRPF38A to partially segregate out of nuclear speckles into foci next to nuclear speckles (Fig. 4, A–D; Fig. S4 A; and Video 2). SON was undetectable in the adjacent MFAP1/PRPF38A foci, as visualized by anti-SON immunostaining (Fig. 4, B and C). The MFAP1/PRPF38A foci that form following transcriptional inhibition are similar in shape and size to the foci observed in GFP-MFAP1- or GFP-PRPF38A-overexpressing cells (Fig. 2, B–D).

Live-cell imaging revealed that these GFP-MFAP1 and GFP-PRPF38A foci that form next to nuclear speckles after RNA pol II transcriptional inhibition are dynamic, disappearing within 1 h following release of the transcription block (Fig. 4, E and F). Their disappearance coincides with the reaccumulation of GFP-MFAP1 or GFP-PRPF38A inside nuclear speckles and restoration of the normal nuclear speckle shape (Fig. 4, E and F; Video 3; and Video 4).

### Nuclear entry of MFAP1 and formation of nuclear foci precedes complete nuclear speckle reformation in early G1

Given MFAP1's possible role in maintaining normal nuclear speckle size, we next investigated the temporal localization of



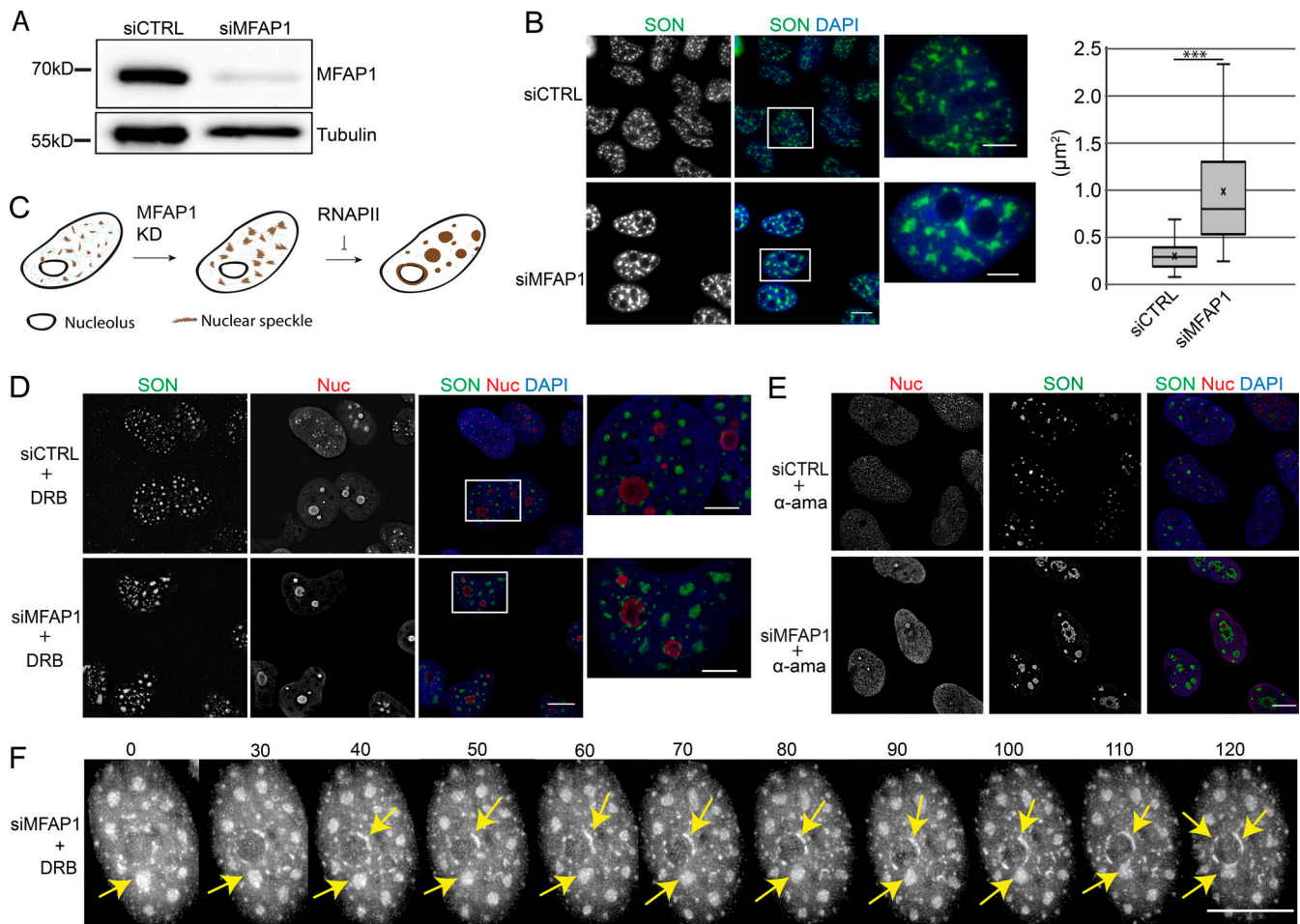


**Figure 3. MFAP1 KD increases nuclear speckle size and changes nuclear distribution of nuclear speckle proteins after transcriptional inhibition.** (A) Western blot showing (top) KD of endogenous MFAP1 protein after siRNA treatment against MFAP1 (siMFAP1) versus control siRNA (siCTRL) in U2OS cells. Tubulin (bottom) is the loading control. (B) SON immunostaining (green) in U2OS cells transfected with siCTRL or siMFAP1. DNA (DAPI) is shown in blue. Boxed areas are magnified on the right. Box plots show nuclear speckle sizes after siMFAP1 versus siCTRL ( $n = 80$  from three independent experiments  $t$  test; \*\*\*,  $P < 0.0001$ ). (C) Schematic depicting increased nuclear speckle size with MFAP1 KD followed by rounding of nuclear speckles after transcriptional inhibition but with redistribution to nucleolar periphery. (D and E) SON (green) and nucleophosmin (Nuc; red) immunostaining with DNA (DAPI, blue) counterstaining of U2OS cells transfected with siCTRL (top) or siMFAP1 (bottom) 48 h before DRB treatment for 2 h (D) or  $\alpha$ -amanitin ( $\alpha$ -ama) overnight treatment (E). Boxed areas in D are magnified on the right. (F) Video stills (Video 1) showing nuclear speckles after addition of DRB to inhibit transcription in MFAP1 KD (siMFAP1) U2OS cells (top of each panel, time in minutes). Arrows (top) indicate nuclear speckle accumulating around nucleolar periphery. Bottom arrows show a larger nuclear speckle merging with nucleolar periphery. Nuclear speckles were visualized with GFP-ZNF207. Scale bars: main panel, 10  $\mu$ m; inset, 5  $\mu$ m.

MFAP1 during mitosis when nuclear speckles first disassemble and then reform.

Nuclear speckles disassemble after initiation of mitosis and their components diffuse throughout the dividing cell (Ferreira et al., 1994). In late metaphase, some nuclear speckle components begin to aggregate into cytoplasmic “mitotic interchromatin granules” (MIGs). MIGs increase in size and number as cells progress into telophase (Ferreira et al., 1994; Prasanth et al., 2003). During late telophase, MIGs then disassemble, and their components are sequentially imported into the nucleus to form nuclear speckles (Prasanth et al., 2003).

We compared GFP-MFAP1 localization versus SON or SC35 immunostaining during these mitotic events. GFP-MFAP1 diffusely localized throughout the cell following initiation of mitosis. In telophase cells, GFP-MFAP1 was mainly concentrated within the nuclei, while SON and SC35 remained within

cytoplasmic MIGs (Fig. 5, A and B). Before nuclear speckles reformed, as assayed by SON or SC35 localization, GFP-MFAP1 was present both diffusely throughout the nucleus and also concentrated in many small, distinct, round foci that did not stain for either SON or SC35 (Fig. 5, A and B; and Fig. S4 B). Similar nuclear foci were observed in telophase cells expressing GFP-PRPF38A (Fig. 5 C). These GFP-MFAP1 foci showed no coilin staining (Fig. 5 D); therefore, they do not correspond to mitotic coiled bodies (Ferreira et al., 1994). However, their appearance and distribution resemble previous reports of the redistribution of U-snrRNPs during mitosis in PtK2 rat kangaroo cells (Spector and Smith, 1986).

We next compared MFAP1 and SON dynamics in live cells during progression through mitosis into early G1. Both GFP-MFAP1 and mCherry-SON became diffusely localized throughout the cytoplasm upon the start of mitosis (Fig. 5 E, Video 5, and

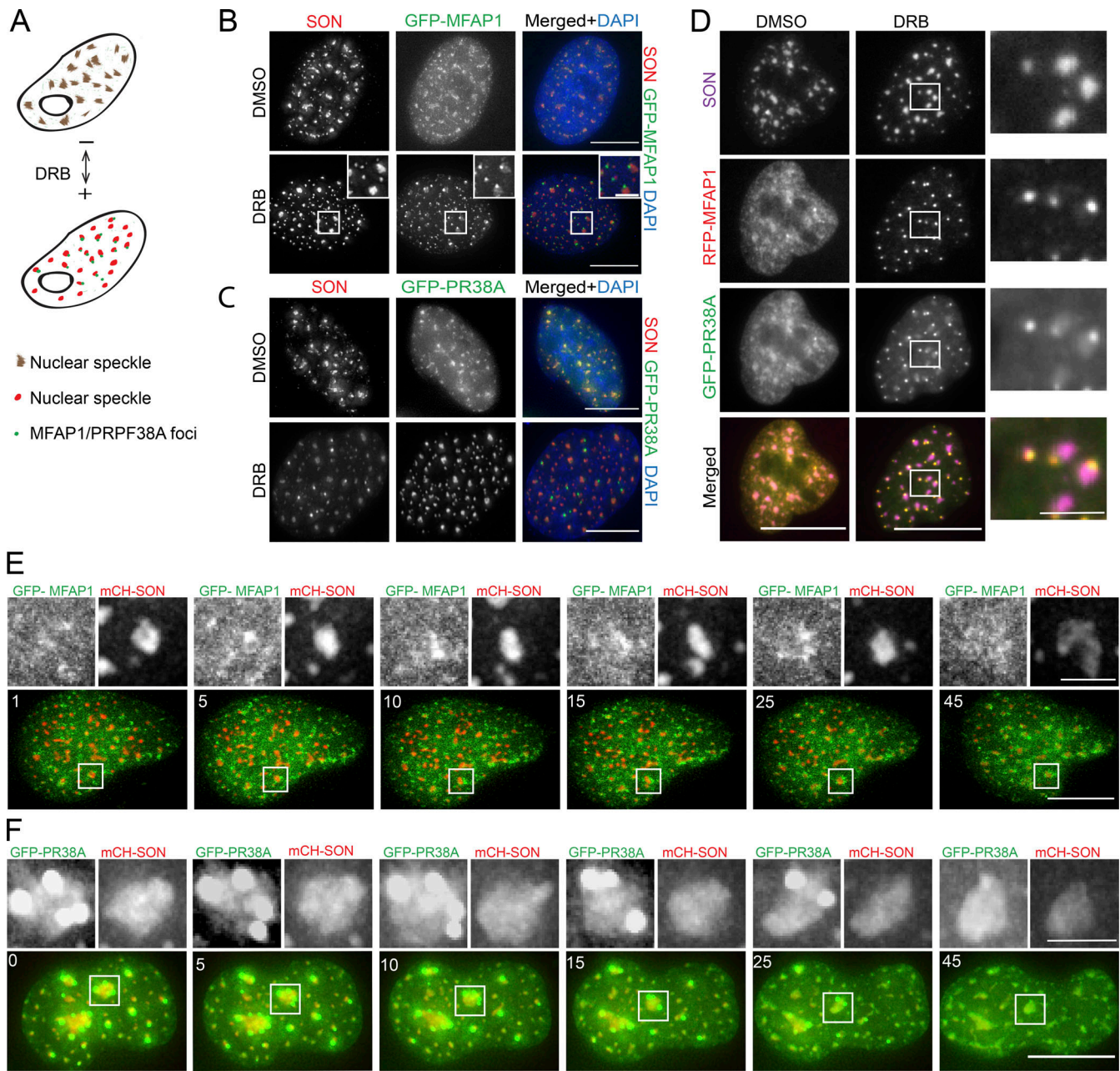


**Figure 4. MFAP1 and PRPF38A segregate out of nuclear speckles and into droplet-like bodies adjacent to nuclear speckles after RNA pol II transcription inhibition.** (A) Schematic depicting MFAP1/PRPF38A (green) before and after treatment with the RNA pol II transcription inhibitor DRB. (B and C) Maximum-intensity projections of optical sections of U2OS cells expressing GFP-MFAP1 (B) or GFP-PRPF38A (C, green; GFP-PRPF38A) treated with either DMSO (top panels) or DRB (bottom panels) for 2 h. Nuclear speckles (red, SON immunostaining) and DNA (blue, DAPI staining) are shown. Insets are magnifications of boxed areas. (D) SON immunostaining (magenta) of U2OS cells coexpressing GFP-PRPF38A (GFP-PRPF38A) and tagRFP-MFAP1 (RFP-MFAP1) treated with either DMSO or DRB. Boxed areas show magnified views (right panels). (E and F) Recovery of GFP-MFAP1 (E, green; Video 3) or GFP-PRPF38A (F, green; Video 4) back into nuclear speckles after release from DRB inhibition. Live cell imaging of U2OS cells coexpressing mCherry-SON after 2-h DRB treatment followed by rinsing with fresh growth media ( $t = 0$ ). Times (1–45 min) are shown in the top left corner. Boxed areas are magnified (top panels) in grayscale. Scale bars: main panel, 10  $\mu\text{m}$ ; inset, 2  $\mu\text{m}$ .

Video 6). In late anaphase and early telophase, when mCherry-SON was mainly present in cytoplasmic MIGs, GFP-MFAP1 already was rapidly accumulating in the reforming nucleus (Fig. 5 E and Video 5). This nuclear accumulation of GFP-MFAP1, lasting ~5 min, was then followed by the formation of distinct nuclear foci (Video 5 and Video 6). Formation of GFP-MFAP1 nuclear foci was followed by the gradual reduction in the size

and number of cytoplasmic MIGs and the increasing colocalization of GFP-MFAP1 and mCherry-SON (Fig. 5 E and Video 5). These results are consistent with previous reports of the sequential entry of nuclear speckle components into the nucleus after mitosis (Prasanth et al., 2003) but show that formation of MFAP1 foci precedes the start of nuclear speckle assembly (Fig. 5). However, our current temporal and spatial resolution

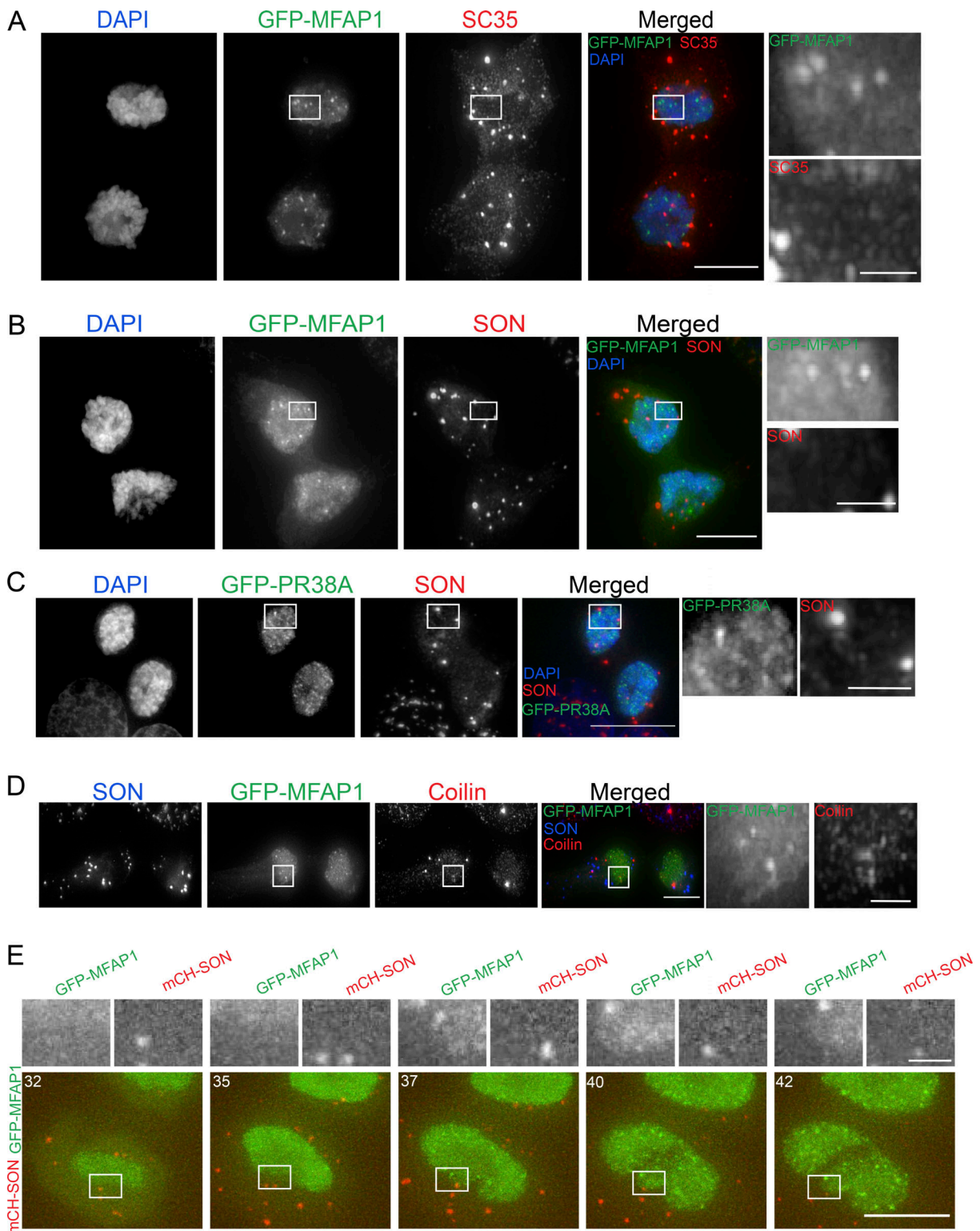


Figure 5. **MFAP1 and PRPF38A nuclear foci appear after mitosis, before nuclear speckle reassembly.** (A and B) Maximum-intensity projections of U2OS telophase daughter cells expressing GFP-MFAP1 (green) and immunostained with either anti-SC35 (A) or anti-SON (B) antibodies (red) to mark nuclear speckles. (C) Maximum-intensity projections of U2OS telophase daughter cells expressing GFP-PRPF38A (GFP-PR38A, green) and immunostained with anti-SON antibody (red). DNA (DAPI) is shown in blue (A–C). (D) Optical section showing U2OS telophase daughter cells expressing GFP-MFAP1 (green) and coimmunostained with antibodies for coilin (red) and SON (blue). Boxed areas are magnified (right panels). (E) Live-cell imaging (Video 5) of telophase U2OS cells coexpressing mCherry-SON (red) and GFP-MFAP1 (green) showing nuclear entry and formation of MFAP1 foci while SON is still present in cytoplasmic foci. Time (in minutes) after start of mitosis is shown in the top left corners. Boxed areas are magnified (top panels) in grayscale. Scale bars: main panels, 10  $\mu$ m; insets, 2  $\mu$ m.

does not allow us to determine whether MFAP1 foci might directly nucleate the reformation of nuclear speckles.

## Discussion

To identify proteins within a specific cellular structure, we combined the TSA proximity-labeling method with a simple ratio approach comparing target and reference cell structures. TSA proximity labeling was followed by affinity pull-down and quantitative MS. This TSA-MS ratio approach compensates for the large diffusion radius of the label-generating free radical, resulting in labeling of many proteins located outside the target cell structure, and allows for the sorting of candidate proteins with a high likelihood of localizing within the target cell structure. We applied TSA-MS ratio to identify proteins enriched in nuclear speckles, using nuclear speckles as the target and centromeres as the reference structures.

Peroxidase-based proximity-labeling methods rely on the diffusion of enzyme-generated free radicals to label proteins. Thus, extraneous proteins may represent a significant fraction of labeled proteins due to the staining radius of the free radical relative to the size of the target structures. For example, the  $\sim 1 \mu\text{m}$  (Chen et al., 2018) estimated staining radius of HRP-generated biotin-tyramide is relatively large and, in the case of centromeres, could overlap with some nuclear speckles. To minimize false positives resulting from this extended TSA labeling radius, we compared the relative abundance of proteins in the nuclear speckles versus centromere pull-down fractions.

This comparison resulted in a significant enrichment of validated nuclear speckle proteins among the top proteins sorted by their SPK-CEN ratio. Specifically, 29 out of the top 30 and 67 out of the top 100 sorted proteins localized to nuclear speckles based on light microscopy. This includes three proteins (MFAP1, PRPF38A, and ZNF207), for which conflicting data existed previously, that we validated here as localized to nuclear speckles using a combination of different fixation conditions and live-cell imaging. The true percentage of nuclear speckle proteins may be even higher, as we demonstrated that formaldehyde fixation perturbs apparent nuclear speckle localization. The percentage of validated nuclear speckle proteins, however, dropped rapidly as the SPK-CEN ratio further decreased.

In contrast, the list of proteins with high centromere ratio (CEN-SPK ratio) was dominated by annotated nucleolar and cytoplasmic proteins. However, this is consistent with the estimated TSA staining radius (Chen et al., 2018) and the observed localization of centromeres adjacent to the nucleolar and nuclear periphery (Carvalho et al., 2001). Centromere and pericentric heterochromatin proteins were present in this sorted list, but they showed lower CEN-SPK ratios than the nucleolar and cytoplasmic contaminants; other centromeric and pericentric heterochromatin proteins were only present in the centromere pull-down fractions.

Thus, the different performance of the ratio sorting approach for identifying the relative enrichment of proteins in centromere versus nuclear speckle pull-down fractions can be explained by the TSA staining radius and the size and location of the centromere and nuclear speckle target bodies. While centromeres were a good reference structure to eliminate false

positives corresponding to nucleoplasmic proteins surrounding both centromeres and nuclear speckles, nuclear speckles were not a suitable reference structure to identify proteins enriched in centromeres. Future applications of TSA-MS ratio will need to use these concepts to select suitably matched target and reference compartments. Previously, we showed that the tyramide free radical-staining radius can be reduced by varying the TSA-staining conditions (Chen et al., 2018). We anticipate that future use of conditions resulting in reduced free radical spreading should further improve TSA-MS ratio results.

Our analysis identified many known nuclear speckle proteins that were absent in the isolated IGC granule proteome (Saitoh et al., 2004), including 20 among the 67 validated nuclear speckle proteins in the top 100 sorted list. Perhaps many of these proteins detected by our approach that were not in the IGC granule proteome correspond to nuclear speckle proteins that are not IGC granule components or granule components that are lost during the IGC granule fractionation procedure.

Consistent with previous work (Saitoh et al., 2004), the majority of the top SPK-CEN ratio-sorted proteins are involved in RNA synthesis or processing (Saitoh et al., 2004). The fraction of proteins involved in RNA metabolism remains high with decreasing SPK-CEN ratio, even while the percentage of validated nuclear speckle proteins falls off sharply after the top 100 sorted proteins. Proteins with low SPK-CEN ratio may have fast on/off rates of nuclear speckle association, reducing their speckle concentration during the slow formaldehyde fixation. Thus, the true nuclear speckle concentration of such proteins may be higher if visualized using other fixation methods or live-cell imaging (Teves et al., 2016), as we demonstrated for ZNF207. Proteins with lower SPK-CEN ratio might also correspond to proteins enriched in regions surrounding nuclear speckles rather than inside the speckles themselves. A last possibility is that these proteins might associate with tyramide-labeled proteins after cell lysis and during pull-down.

Nuclear speckles are now thought to form through liquid-liquid phase separation mediated by protein-protein and protein-RNA interactions (Galganski et al., 2017). Proteins containing low-complexity disordered domains readily form liquid-like bodies both in vivo and in vitro (Altmeyer et al., 2015; Jiang et al., 2015; Patel et al., 2015). However, pure liquid-phase separated bodies should be perfectly round, unlike the shape of nuclear speckles in nonperturbed cells. What nuclear speckle components might contribute to these deviations from a pure liquid-like behavior, conferring nonround shape and nonliquid-like behavior to nuclear speckles, are currently unknown.

Here, we identified MFAP1 as a possible regulator of nuclear speckle size and anchoring of nuclear speckles to chromatin. Specifically, we demonstrated enlargement of nuclear speckles after MFAP1 KD. Conversely, after transcription inhibition both MFAP1 and PRPF38A partially segregate into dynamic foci next to nuclear speckles, with this segregation correlating with the rounding of nuclear speckles generally seen after transcription inhibition (Galganski et al., 2017). Combining RNA pol II transcription inhibition with MFAP1-KD cells caused fusion of some nuclear speckles into fewer and larger nuclear speckles, as well as nuclear speckle fusion with the nucleolar periphery.

Finally, MFAP1, possibly with PRPF38A, forms nuclear bodies distinct from nuclear speckles. When overexpressed, both MFAP1 and PRPF38A segregate out of nuclear speckles, forming round nuclear bodies in the nucleoplasm distinct from nuclear speckles, defined by either SC35 or SON staining. As described in the previous paragraph, transcriptional inhibition also causes MFAP1 and PRPF38A to segregate out of but adjacent to nuclear speckles. Interestingly, both MFAP1 and PRPF38A reenter telophase nuclei before import of other nuclear speckle markers such as SC35 and SON. In these early telophase nuclei, MFAP1 and PRPF38A then condense to form round nuclear bodies similar in size and shape to those observed after either overexpression or transcriptional inhibition. Future experiments will be needed to test what other nuclear speckle proteins cosegregate within these MFAP1/PRPF38A bodies and whether they may actually nucleate the reformation of nuclear speckles after mitosis.

In summary, comparing the proteomes of multiple subcellular structures within the crowded nucleoplasm allows improved identification of proteins in different membrane-less cellular compartments. Furthermore, combining proximity-labeling methods with different effective staining radii should allow the probing of different size volumes surrounding the staining target. This should help improve the true positive hit rate while also helping to identify proteins in the same cell structure that may not be in actual molecular contact. Meanwhile, identification of new nuclear speckle proteins should lead to improved structural and functional dissection of nuclear speckles, as illustrated with our identification of the changes in nuclear speckle size, shape, and nuclear distribution produced after manipulating MFAP1 levels.

## Materials and methods

### Cell culture, plasmid constructs, and transfections

U2OS and Tig3 cells were cultured in DMEM (Thermo Fisher Scientific) supplemented with 10% bovine growth serum (HyClone). CHO cells were cultured in Ham's F12 media (Thermo Fisher Scientific) supplemented with FBS (MilliporeSigma). Penicillin-streptomycin (Thermo Fisher Scientific) was added to all growth media, and cells were incubated in a 37°C humidified incubator with 5% CO<sub>2</sub>. For DNA cloning, total RNA was extracted from U2OS cells using RNeasy kit (Qiagen). Approximately 1 µg total RNA was reverse transcribed into cDNA using the Protoscript First Strand cDNA Synthesis Kit (New England Biolabs). Unless otherwise stated, all GFP constructs were cloned, using a PCR-based strategy, into the Clontech pGFP-C1 backbone (Clontech). All mCherry constructs were based on the pmCherry-C1 backbone (Clontech). pCIBN-hTRF2-tagRFP-T was a gift from Karsten Rippe (University of Heidelberg, Heidelberg, Germany; plasmid 103812; Addgene). TagRFP-MFAP1 was modified from GFP-MFAP1 construct by replacing the GFP open reading frame with TagRFP open reading frame using AgeI and XhoI restriction sites. All constructs were sequenced and verified before use. DNA constructs were transfected using the Lipofectamine 2000 Transfection Reagent (Thermo Fisher Scientific) and following the manufacturer's instructions with minor modifications. Briefly, cells in 6-well plates were

transfected with 0.5 µg plasmid DNA, and 24-well plates were transfected with 0.1 µg plasmid DNA. Transfection complexes were prepared by separately diluting plasmid DNA and Lipofectamine 2000 reagent in appropriate volumes of OptiMEM (Thermo Fisher Scientific). Diluted DNA and Lipofectamine 2000 transfection reagent were mixed and incubated for 5 min at room temperature to form transfection mix. Transfection mix was added onto cells in complete growth media, and cells were incubated at 37°C and either analyzed after 24 h or, for long-term culturing, drugs for selection were added.

### Antibodies

The following primary antibodies were used in this study: anti-CENPA (AB13939; Abcam), anti-SC35 (S4045; MilliporeSigma), anti-MFAP1 (HPA042370; MilliporeSigma), anti-SRRM2 (PA5-68009; Thermo Fisher Scientific), anti-ZNF207 (HPA017013; MilliporeSigma), anti-HP1α (H2164; MilliporeSigma), anti-β Tubulin (AB18207; Abcam), anti-FITC (200-002-037; Jackson ImmunoResearch), custom-made anti-SON (Chen et al., 2018; PACIFIC10700; Pacific Immunology), anti-Nucleophosmin (AB86712; Abcam), anti-nucleolin (AB70493; Abcam), anti-Coilin (Ab87913; Abcam), and anti-PRPF38A (PA5-62730; Thermo Fisher Scientific). Secondary antibodies used were goat anti-mouse HRP (115-035-062; Jackson ImmunoResearch), goat anti-rabbit HRP (111-035-144; Jackson ImmunoResearch), goat anti-mouse FITC (111-095-144; Jackson ImmunoResearch), and goat anti-rabbit Texas red (115-075-146; Jackson ImmunoResearch).

### RNA interference

The following RNA duplexes were used for RNAi: ON-TARGETplus nontargeting control siRNA #1 (D-001810-01-05; Dharmacon), human MFAP1 (D-020071-03-0002: 5'-AAGUGA AGGUAAGCGUUA-3'; Dharmacon), human MFAP1 3' UTR (D-020071-17-0002: 5'-GGAGUAAUAUACCCGGAAA-3'; Dharmacon), mouse Mfap1a (D-063511-01-0002: 5'-UAAGAAAGCUAA GGAACAA-3'; Dharmacon), human SRRM2 (D-015368-01: 5'-GAGCAAUUCUCAAACAUCA-3'; D-015368-03: 5'-AAAGAAUGU CCACAAGUA-3'; D-015368-05: 5'-GGAAUGAAAGAUUACCUA-3'; D-015368-006: 5'-GACAGCAAUUCGACUAU-3'; Dharmacon), and human PRPF38A (D-014833-02-0002: 5'-CGAUAA AGCCAUGGAGUUA-3'; Dharmacon). ZNF207 siRNA oligo was used in a previous study (Jiang et al., 2015; 5'-GCCUGCUACACU UACAACAACUAU-3'; Invitrogen). The sequence targeting the mouse Mfap1a (D-063511-01-0002) exactly matches the region in CHO cells and was thus used to knock down Mfap1 in CHO cells. All siRNAs were transfected at a concentration of 10 nM using the Lipofectamine RNAiMax transfection reagent (Thermo Fisher Scientific) and following the manufacturer's directions. Briefly, cells were seeded overnight, and transfection complexes were prepared by separately diluting 10 nM siRNA and appropriate volume of Lipofectamine RNAiMAX transfection reagent in OptiMEM. Diluted siRNA and RNAiMAX transfection reagent were mixed and incubated for 5 min to form transfection complexes. Transfection complexes were added onto cells in complete growth media and cells were incubated for 72–96 h before cells were analyzed. Western blotting was used to determine KD of proteins.

### Chemical treatments

The following chemical inhibitors were used in this study to inhibit RNA pol II transcription: 5,6-dichloro-1- $\beta$ -D-ribofuranosylbenzimidazole (DRB; D1916) was purchased from MilliporeSigma and  $\alpha$ -amanitin (CAS 23109-05-9) was purchased from Santa Cruz Biotechnology. All inhibitors were dissolved in DMSO and used at the following final concentrations: DRB, 50  $\mu$ g/ml;  $\alpha$ -amanitin, 10  $\mu$ g/ml. For washout experiments with DRB, cells were incubated with DRB for 2 h before cells were rinsed at least three times with prewarmed complete growth media.

### Immunostaining, microscopy, and image processing

Cells were seeded on coverslips in appropriate wells, and where indicated, cells were treated before fixing with either 100% ice-cold methanol at  $-20^{\circ}\text{C}$  or 4% PFA (MilliporeSigma) in PBS at room temperature. All fixations were for 20 min, and cells were rinsed at least three times with PBS after fixation. PFA-fixed cells were permeabilized with 0.1% Triton X-100 (MilliporeSigma) for 30 min at room temperature. Cells were blocked for 1 h at room temperature in blocking buffer consisting of 5% goat serum (MilliporeSigma) and 0.1% Triton X-100 in PBS before incubation with appropriate dilution of primary antibody, in blocking buffer, for 1 h at room temperature or overnight at  $+4^{\circ}\text{C}$ . Cells were rinsed three times with wash buffer (0.1% Triton X-100 in PBS) and incubated at room temperature with fluorescent-conjugated secondary antibody diluted in blocking buffer. After 1 h, cells were rinsed three times with wash buffer and mounted using Mowiol (Calbiochem) containing 1,4-diazabicyclo [2.2.2] octane (MilliporeSigma). DAPI (MilliporeSigma) was added to stain DNA in the nucleus. All images of fixed cells were acquired using a DeltaVision microscope equipped with a Xenon lamp, 60 $\times$  1.4 NA oil-immersion objective lens (Olympus) and CoolSNAP HQ charge-coupled device camera (Roper Scientific) and the SoftWorx imaging software (GE Healthcare). Where necessary, images were deconvolved and projected into 2D using the maximum intensity algorithm in SoftWorx imaging software. Where applicable, images were exported into TIFF and processed using FIJI (ImageJ). Nuclear speckle areas were also measured using FIJI, and time-lapse videos were converted into MP4 with VLC media player.

### Time-lapse microscopy

For live imaging, cells were seeded in 35-cm glass-bottom dishes (MatTek Corporation) and treated as required. Imaging was performed at  $37^{\circ}\text{C}$  in 5%  $\text{CO}_2$  chamber attached to a V3 OMX microscope (GE Healthcare) equipped with a 100 $\times$  1.4 NA oil-immersion objective (Olympus) and an electron multiplying charge-coupled device camera (Photometrics). We collected image stacks, deconvolved and projected into 2D using the maximum intensity projection algorithm in the SoftWorx software (GE Healthcare). Where necessary, DNA was stained using the SiR-DNA kit (Cytoskeleton).

### Western blotting

Proteins were resolved in 8% or 10% SDS-PAGE gels and transferred into nitrocellulose membranes (Bio Rad laboratories). Membranes were blocked for 1 h at room temperature with

blocking buffer (5% nonfat milk, 0.1% Tween 20 in PBS) before membranes were incubated, overnight at  $4^{\circ}\text{C}$ , with gentle rocking, in primary antibodies diluted in blocking buffer. Membranes were washed three times 10 min in wash buffer (0.1% Tween 20 in PBS) at room temperature before membranes were incubated with HRP-conjugated secondary antibodies at room temperature for 1 h in blocking buffer. Membranes were washed 3  $\times$  10 min in wash buffer, incubated in Immobilon Western HRP Substrate (Millipore) for 5 min before protein bands were detected using iBright Imaging System (Thermo Fisher Scientific). Tubulin was detected as the loading control.

### Tyramide-FITC conjugation and TSA reaction

While tyramide-fluorescein (FITC) is commercially available (for example, PerkinElmer, # NEL741001KT), we instead performed tyramide-fluorescein conjugation as previously described (Hopman et al., 1998). Fluorescein-NHS ester was purchased from Thermo Fisher Scientific; and tyramine hydrochloride (tyramide), dimethyl formamide (DMF), and triethylamine were purchased from MilliporeSigma. Fluorescein-NHS stock solution (21 mM) was prepared in DMF. Tyramide-hydrochloride (HCL) stock solution (58 mM) was prepared in DMF containing 71 mM triethylamine. Equal amounts of fluorescein-NHS in the fluorescein-NHS stock solution and tyramide-HCL in the tyramide-HCL stock solution were combined and the mixture was incubated in the dark for 2 h at room temperature. The conjugated tyramide-FITC was diluted to 1 mg/ml with ethanol and stored in dark at  $-20^{\circ}\text{C}$ . The TSA protocol was modified from Chen et al. (2018). U2OS cells were grown to 90% confluency in 15-cm cell culture dishes. Cells were fixed with 1% PFA in PBS at room temperature for 20 min. Cells were rinsed for 10 min with 0.25 M glycine to quench free aldehydes and further rinsed with PBS, scrapped using cell lifter (Thermo Fisher Scientific), and transferred into a 1.5-ml tube for subsequent processing. From this point on, all washes were done by suspending cells in 1 ml PBST (0.1% Triton X-100 in PBS) followed by 3-min centrifugation at 3,000 rpm in room temperature. Cells were permeabilized with 0.5% Triton X-100 for 30 min at room temperature under gentle rotation. Cells were washed three times and suspended in 1.5%  $\text{H}_2\text{O}_2$  (MilliporeSigma) and incubated at room temperature, with gentle rotation, to quench the endogenous peroxidase. After 1 h, cells were rinsed three times with PBST and blocked for 1 h at room temperature in blocking buffer (5% goat serum in PBST). Typically, cells were suspended in primary antibodies diluted in 1 ml blocking buffer at 2  $\mu$ g per 20 million cells and incubated overnight at  $4^{\circ}\text{C}$  with gentle rotation. Cells were rinsed three times with PBST and suspended in HRP-conjugated secondary antibody at 2  $\mu$ g per 20 million cells in blocking buffer and incubated overnight at  $4^{\circ}\text{C}$ . Cells were rinsed three times with PBST and suspended in TSA reaction buffer (0.1  $\mu$ g/ml tyramide-fluorescein in PBS and 0.015%  $\text{H}_2\text{O}_2$ ) for 10 min before cells were rinsed three times with PBST. To verify the TSA labeling reaction,  $\sim 5$   $\mu$ l cell pellet was mounted on cover glasses, using Mowiol 1,4-diazabicyclo [2.2.2] octane, for light microscopy. Approximately 150 million cells were processed per antibody for each MS run.

### Pull-down of tyramide-FITC-labeled proteins

To affinity purify and enrich fluorescein (FITC)-labeled proteins, we used the Pierce Direct IP kit (#26148; Thermo Fisher Scientific) to couple anti-FITC antibody to agarose beads following the manufacturer's instructions with some modifications. We used 10  $\mu\text{g}$  anti-FITC antibody and 25  $\mu\text{l}$  Pierce AminoLink Plus Coupling Resin slurry in the coupling reaction. After the coupling reaction, columns containing anti-FITC coupled beads were either directly used for the pull-down of FITC-labeled proteins or stored at +4°C in Pierce coupling buffer with 0.02% sodium azide until needed. For the pull-down of FITC-labeled proteins, after TSA reaction, cells were rinsed once with coupling buffer and suspended in 500  $\mu\text{l}$  ice-cold Pierce lysis buffer supplemented with protease inhibitor cocktail (MilliporeSigma) and DNase I (New England Biolabs). Cell suspension was incubated on ice for 30 min and vortexed every 5–10 min. Cell suspension was passed through a 25G needle (BD Biosciences) attached to a 1-ml syringe (BD Biosciences) to break larger cell clumps. Cells were sonicated at 4°C using the Bioruptor Pico sonicator (Diagenode) to obtain clear or evenly cloudy lysates. Lysates were centrifuged at 16,000 rpm for 10 min at 4°C to pellet cell debris. Equal amounts of the supernatants, as determined using the BCA Assay Kit (Thermo Fisher Scientific) from either anti-SC35 TSA or anti-CENPA TSA reaction, were cleared for 1 h at 4°C using Pierce Control Agarose Resin. Cleared lysates were loaded onto Pierce Spin Columns containing anti-FITC-coupled Pierce AminoLink plus coupling resin and incubated overnight at +4°C with gentle end-over-end rotation. Beads were washed three times with ice-cold wash buffer supplemented with protease inhibitor and once with 100  $\mu\text{l}$  Pierce conditioning buffer. Beads were eluted in a total volume of 50  $\mu\text{l}$  of Pierce elution buffer. Approximately 20  $\mu\text{l}$  eluate was boiled in SDS-PAGE sample loading buffer for 10 min at 100°C and saved for Western blotting; the other 30  $\mu\text{l}$  was saved for in-solution trypsin digestion and MS.

### MS

Eluted proteins were reduced with Tris (2-carboxyethyl) phosphine (MilliporeSigma), alkylated with Iodoacetamide (MilliporeSigma), and digested with Lys C/Trypsin (Thermo Fisher Scientific) overnight. The digested samples were desalted by HPLC using an Optimize Technologies C8 microtrap. Samples were resuspended in 0.2% formic acid and directly loaded onto a PicoFrit column (New Objective) packed in house with ReproSil-Pur C18AQ 1.9  $\mu\text{m}$  resin (120 Å pore size; Dr. Maisch GmbH). The 25 cm  $\times$  50  $\mu\text{m}$  ID column was heated to 60°C. The peptides were separated with a 120-min gradient at a flow rate of 220 nl/min using a nanoflow LC system, EASY-nLC 1200, (Thermo Fisher Scientific). The gradient was as follows: 2–6% solvent B (7.5 min), 6–25% B (82.5 min), and 25–40% B (30 min), and 40–100% B (9 min). Solvent A consisted of 97.8% H<sub>2</sub>O, 2% acetonitrile, and 0.2% formic acid and solvent B consisted of 19.8% H<sub>2</sub>O, 80% acetonitrile, and 0.2% formic acid. The separated peptides were ionized by a Nanospray Flex ion source and subjected to MS/MS analysis using a QExactive HF Orbitrap mass spectrometer (Thermo Fisher Scientific). The QExactive HF Orbitrap was operated in data-dependent mode with the Tune (version 2.7

SP1build 2659) instrument control software. Spray voltage was set to 2.5 kV, S-lens RF level at 50, and heated capillary at 275°C. Full scan resolution was set to 60,000 at  $m/z$  200. Full scan target was  $3 \times 10^6$  with a maximum injection time of 15 ms. Mass range was set to 300–1,650  $m/z$ . For data-dependent MS2 scans, the loop count was 12, target value was set at  $10^5$ , and intensity threshold was kept at  $10^5$ . Isolation width was set at 1.2  $m/z$ , and a fixed first mass of 100 was used. Normalized collision energy was set at 28. Peptide match was set to off, and isotope exclusion was on. Data acquisition was controlled by Xcalibur (4.0.27.13).

### LFQ of MS data

Raw data were analyzed using MaxQuant (version 1.6.5.0; Cox and Mann, 2008). Spectra were searched against UniProt human entries (74,487 sequences) and a contaminant protein database (247 sequences). A decoy database was used to establish score thresholds to achieve a 1% protein and peptide false discovery rate. Variable modifications searched were protein N-terminal acetylation and methionine oxidation. Carbamidomethylation was specified as a fixed modification of cysteine. Trypsin was the specified digestion enzyme with up to two missed cleavages allowed. LFQ and match-between-runs were enabled (Cox et al., 2014).

### Online supplemental material

Fig. S1 shows TSA labeling of proteins, including chemical structure of tyramide-FITC, Western blots, and protein gels after TSA labeling. Fig. S2 shows data analysis, functional annotation, and validation of potential nuclear speckle proteins, including analysis of MS data and demonstration of loss of ZNF207 and MFAP1 from speckles after PFA fixation. Fig. S3 shows that MFAP1 KD specifically increases nuclear speckle size. Fig. S4 shows nuclear distribution of MFAP1 relative to nuclear speckles as function of DRB treatment and also in mitosis. Table S1 shows MS data. Video 1 shows that nuclear speckles in MFAP1-depleted cells relocate to nucleolar periphery after DRB treatment (related to Fig. 3 F). Video 2 shows that GFP-MFAP1 segregates into foci adjacent to nuclear speckles after DRB treatment. Video 3 shows that reversal of RNA pol II transcription inhibition results in disappearance of MFAP1-positive droplet-like foci adjacent to nuclear speckles (related to Fig. 4 E). Video 4 shows that reversal of RNA pol II transcription inhibition results in disappearance of GFP-PRPF38A droplet-like foci adjacent to nuclear speckles (related to Fig. 4 F). Video 5 shows that GFP-MFAP1 reenters nucleus and forms droplet-like foci before reentry of SON protein and nuclear speckle reassembly after mitosis (related to Fig. 5 E). Video 6 shows that GFP-MFAP1 localizes and accumulates into foci in the nucleus before complete chromatin decondensation (related to Fig. 5 E).

### Acknowledgments

The authors thank all members of the Belmont laboratory for suggestions and advice.

A.S. Belmont acknowledges support from National Institutes of Health R01 grant GM58460. The California Institute of Technology Proteome Exploration Laboratory is supported by

the Beckman Institute and National Institutes of Health grant 1S10OD02001301. Light microscopy was performed in the Department of Molecular and Cellular Biology Light Microscopy Facility, funded with support from the Carver Foundation.

The authors declare no competing financial interests.

Author contributions: J. Dopie and A.S. Belmont conceived of and designed the research plan. J. Dopie designed the experimental plan and performed all experiments. A. Moradian and M.J. Sweredoski provided advice on preparation of samples for MS, performed MS, provided analysis of MS data, and advised on the ratio analysis approach. The manuscript was written by J. Dopie and A.S. Belmont with input from A. Moradian and M.J. Sweredoski regarding the MS.

Submitted: 29 October 2019

Revised: 3 April 2020

Accepted: 13 May 2020

## References

- Agafonov, D.E., J. Deckert, E. Wolf, P. Odenwalder, S. Bessonov, C.L. Will, H. Urlaub, and R. Luhrmann. 2011. Semiquantitative proteomic analysis of the human spliceosome via a novel two-dimensional gel electrophoresis method. *Mol. Cell. Biol.* 31:2667–2682. <https://doi.org/10.1128/MCB.05266-11>
- Altmeyer, M., K.J. Neelsen, F. Teloni, I. Pozdnyakova, S. Pellegrino, M. Grofte, M.D. Rask, W. Streicher, S. Jungmichel, M.L. Nielsen, et al. 2015. Liquid demixing of intrinsically disordered proteins is seeded by poly(ADP-ribose). *Nat. Commun.* 6:8088. <https://doi.org/10.1038/ncomms9088>
- Andersen, D.S., and N. Tapon. 2008. Drosophila MFAP1 is required for pre-mRNA processing and G2/M progression. *J. Biol. Chem.* 283:31256–31267. <https://doi.org/10.1074/jbc.M803512200>
- Baldin, V., M. Militello, Y. Thomas, C. Doucet, W. Fic, S. Boireau, I. Jariel-Encontre, M. Piechaczyk, E. Bertrand, J. Tazi, et al. 2008. A novel role for PA28 $\gamma$ -proteasome in nuclear speckle organization and SR protein trafficking. *Mol. Biol. Cell.* 19:1706–1716. <https://doi.org/10.1091/mbc.e07-07-0637>
- Bar, D.Z., K. Atkatsch, U. Tavarez, M.R. Erdos, Y. Gruenbaum, and F.S. Collins. 2018. Biotinylation by antibody recognition—a method for proximity labeling. *Nat. Methods.* 15:127–133. <https://doi.org/10.1038/nmeth.4533>
- Bell, A.W., M.A. Ward, W.P. Blackstock, H.N.M. Freeman, J.S. Choudhary, A.P. Lewis, D. Chotai, A. Fazel, J.N. Gushue, J. Paiement, et al. 2001. Proteomics characterization of abundant Golgi membrane proteins. *J. Biol. Chem.* 276:5152–5165. <https://doi.org/10.1074/jbc.M006143200>
- Bertram, K., D.E. Agafonov, O. Dybkov, D. Haselbach, M.N. Leelaram, C.L. Will, H. Urlaub, B. Kastner, R. Luhrmann, and H. Stark. 2017. Cryo-EM Structure of a Pre-catalytic Human Spliceosome Primed for Activation. *Cell.* 170:701–713.e11. <https://doi.org/10.1016/j.cell.2017.07.011>
- Blencowe, B.J., G. Bauren, A.G. Eldridge, R. Issner, J.A. Nickerson, E. Rosonina, and P.A. Sharp. 2000. The SRm160/300 splicing coactivator subunits. *RNA.* 6:111–120. <https://doi.org/10.1017/S1355838200991982>
- Bobrow, M.N., T.D. Harris, K.J. Shaughnessy, and G.J. Litt. 1989. Catalyzed reporter deposition, a novel method of signal amplification. Application to immunoassays. *J. Immunol. Methods.* 125:279–285. [https://doi.org/10.1016/0022-1759\(89\)90104-X](https://doi.org/10.1016/0022-1759(89)90104-X)
- Bobrow, M.N., K.J. Shaughnessy, and G.J. Litt. 1991. Catalyzed reporter deposition, a novel method of signal amplification. II. Application to membrane immunoassays. *J. Immunol. Methods.* 137:103–112. [https://doi.org/10.1016/0022-1759\(91\)90399-Z](https://doi.org/10.1016/0022-1759(91)90399-Z)
- Burns, C.G., R. Ohi, A.R. Krainer, and K.L. Gould. 1999. Evidence that Myb-related CDC5 proteins are required for pre-mRNA splicing. *Proc. Natl. Acad. Sci. USA.* 96:13789–13794. <https://doi.org/10.1073/pnas.96.24.13789>
- Caceres, J.F., T. Misteli, G.R. Sreaton, D.L. Spector, and A.R. Krainer. 1997. Role of the modular domains of SR proteins in subnuclear localization and alternative splicing specificity. *J. Cell Biol.* 138:225–238. <https://doi.org/10.1083/jcb.138.2.225>
- Carter, K.C., K.L. Taneja, and J.B. Lawrence. 1991. Discrete nuclear domains of poly(A) RNA and their relationship to the functional organization of the nucleus. *J. Cell Biol.* 115:1191–1202. <https://doi.org/10.1083/jcb.115.5.1191>
- Carter, D., L. Chakalova, C.S. Osborne, Y.F. Dai, and P. Fraser. 2002. Long-range chromatin regulatory interactions in vivo. *Nat. Genet.* 32:623–626. <https://doi.org/10.1038/ng1051>
- Carvalho, C., H.M. Pereira, J. Ferreira, C. Pina, D. Mendonça, A.C. Rosa, and M. Carmo-Fonseca. 2001. Chromosomal G-dark bands determine the spatial organization of centromeric heterochromatin in the nucleus. *Mol. Biol. Cell.* 12:3563–3572. <https://doi.org/10.1091/mbc.12.11.3563>
- Chen, Y., Y. Zhang, Y. Wang, L. Zhang, E.K. Brinkman, S.A. Adam, R. Goldman, B. van Steensel, J. Ma, and A.S. Belmont. 2018. Mapping 3D genome organization relative to nuclear compartments using TSA-Seq as a cytological ruler. *J. Cell Biol.* 217:4025–4048. <https://doi.org/10.1083/jcb.201807108>
- Chiara, M.D., P. Champion-Arnaud, M. Buvoli, B. Nadal-Ginard, and R. Reed. 1994. Specific protein-protein interactions between the essential mammalian spliceosome-associated proteins SAP 61 and SAP 114. *Proc. Natl. Acad. Sci. USA.* 91:6403–6407. <https://doi.org/10.1073/pnas.91.14.6403>
- Cox, J., and M. Mann. 2008. MaxQuant enables high peptide identification rates, individualized p.p.b.-range mass accuracies and proteome-wide protein quantification. *Nat. Biotechnol.* 26:1367–1372. <https://doi.org/10.1038/nbt.1511>
- Cox, J., M.Y. Hein, C.A. Luber, I. Paron, N. Nagaraj, and M. Mann. 2014. Accurate proteome-wide label-free quantification by delayed normalization and maximal peptide ratio extraction, termed MaxLFQ. *Mol. Cell. Proteomics.* 13:2513–2526. <https://doi.org/10.1074/mcp.M113.031591>
- Croze, E.M., and D.J. Morre. 1984. Isolation of plasma membrane, golgi apparatus, and endoplasmic reticulum fractions from single homogenates of mouse liver. *J. Cell. Physiol.* 119:46–57. <https://doi.org/10.1002/jcp.1041190109>
- Fakan, S., and E. Puvion. 1980. The Ultrastructural Visualization of Nucleolar and Extranucleolar RNA Synthesis and Distribution. This Article Is Dedicated to the Memory of Dr. Wilhelm Bernhard. In *International Review of Cytology*. Vol. 65. G.H. Bourne, and J.F. Danielli, editors. Academic Press. pp. 255–299.
- Ferreira, J.A., M. Carmo-Fonseca, and A.I. Lamond. 1994. Differential interaction of splicing snRNPs with coiled bodies and interchromatin granules during mitosis and assembly of daughter cell nuclei. *J. Cell Biol.* 126:11–23. <https://doi.org/10.1083/jcb.126.1.11>
- Fodor, B.D., N. Shukeir, G. Reuter, and T. Jenuwein. 2010. Mammalian Su(-var) genes in chromatin control. *Annu. Rev. Cell Dev. Biol.* 26:471–501. <https://doi.org/10.1146/annurev.cellbio.042308.113225>
- Fu, X.-D., and T. Maniatis. 1990. Factor required for mammalian spliceosome assembly is localized to discrete regions in the nucleus. *Nature.* 343:437–441. <https://doi.org/10.1038/343437a0>
- Fu, X.D., and T. Maniatis. 1992. Isolation of a complementary DNA that encodes the mammalian splicing factor SC35. *Science.* 256:535–538. <https://doi.org/10.1126/science.1373910>
- Galganski, L., M.O. Urbanek, and W.J. Krzyzosiak. 2017. Nuclear speckles: molecular organization, biological function and role in disease. *Nucleic Acids Res.* 45:10350–10368. <https://doi.org/10.1093/nar/gkx759>
- Hopman, A.H., F.C. Ramaekers, and E.J. Speel. 1998. Rapid synthesis of biotin-, digoxigenin-, trinitrophenyl-, and fluorochrome-labeled tyramides and their application for In situ hybridization using CARD amplification. *J. Histochem. Cytochem.* 46:771–777. <https://doi.org/10.1177/002215549804600611>
- Horiuchi, K., T. Kawamura, H. Iwanari, R. Ohashi, M. Naito, T. Kodama, and T. Hamakubo. 2013. Identification of Wilms’ tumor 1-associating protein complex and its role in alternative splicing and the cell cycle. *J. Biol. Chem.* 288:33292–33302. <https://doi.org/10.1074/jbc.M113.500397>
- Howell, V.M., J.M. Jones, S.K. Bergren, L. Li, A.C. Billi, M.R. Avenarius, and M.H. Meisler. 2007. Evidence for a direct role of the disease modifier SCNMI in splicing. *Hum. Mol. Genet.* 16:2506–2516. <https://doi.org/10.1093/hmg/ddm206>
- Huang, C.-J., F. Ferfaglia, F. Raleff, and A. Kramer. 2011. Interaction domains and nuclear targeting signals in subunits of the U2 small nuclear ribonucleoprotein particle-associated splicing factor SF3a. *J. Biol. Chem.* 286:13106–13114. <https://doi.org/10.1074/jbc.M110.201491>
- Imai, H., E.K. Chan, K. Kiyosawa, X.D. Fu, and E.M. Tan. 1993. Novel nuclear autoantigen with splicing factor motifs identified with antibody from hepatocellular carcinoma. *J. Clin. Invest.* 92:2419–2426. <https://doi.org/10.1172/JCI116848>
- Inoue, A., K. Tsugawa, K. Tokunaga, K.P. Takahashi, S. Uni, M. Kimura, K. Nishio, N. Yamamoto, K. Honda, T. Watanabe, et al. 2008. Si-1 nuclear domains: characterization and dynamics as a function of transcriptional activity. *Biol. Cell.* 100:523–535. <https://doi.org/10.1042/BC20070142>



- Jiang, H., S. Wang, Y. Huang, X. He, H. Cui, X. Zhu, and Y. Zheng. 2015. Phase transition of spindle-associated protein regulate spindle apparatus assembly. *Cell*. 163:108–122. <https://doi.org/10.1016/j.cell.2015.08.010>
- Kang, J., J. Chaudhary, H. Dong, S. Kim, C.A. Brautigam, and H. Yu. 2011. Mitotic centromeric targeting of HPI and its binding to Sgol are dispensable for sister-chromatid cohesion in human cells. *Mol. Biol. Cell*. 22:1181–1190. <https://doi.org/10.1091/mbc.e11-01-0009>
- Kim, D.I., K.C. Birendra, W. Zhu, K. Motamedchaboki, V. Doye, and K.J. Roux. 2014. Probing nuclear pore complex architecture with proximity-dependent biotinylation. *Proc. Natl. Acad. Sci. USA*. 111:E2453–E2461.
- Kim, J., K.Y. Han, N. Khanna, T. Ha, and A.S. Belmont. 2019. Nuclear speckle fusion via long-range directional motion regulates speckle morphology after transcriptional inhibition. *J. Cell Sci.* 132. <https://doi.org/10.1242/jcs.226563>
- Ko, T.K., E. Kelly, and J. Pines. 2001. CrkRS, a novel conserved Cdc2-related protein kinase that colocalises with SC35 speckles. *J. Cell Sci.* 114: 2591–2603.
- Kruhlik, M.J., M.A. Lever, W. Fischle, E. Verdin, D.P. Bazett-Jones, and M.J. Hendzel. 2000. Reduced mobility of the alternate splicing factor (ASF) through the nucleoplasm and steady state speckle compartments. *J. Cell Biol.* 150:41–51. <https://doi.org/10.1083/jcb.150.1.41>
- Leung, S.W., L.H. Apponi, O.E. Cornejo, C.M. Kitchen, S.R. Valentini, G.K. Pavlath, C.M. Dunham, and A.H. Corbett. 2009. Splice variants of the human ZC3H14 gene generate multiple isoforms of a zinc finger poly-adenosine RNA binding protein. *Gene*. 439:71–78. <https://doi.org/10.1016/j.gene.2009.02.022>
- Li, J.F., L.D. Liu, S.H. Ma, Y.C. Che, L.C. Wang, C.H. Dong, H.L. Zhao, Y. Liao, and Q.H. Li. 2004. HTRP—an immediate-early gene product induced by HSV1 infection in human embryo fibroblasts, is involved in cellular corepressors. *J. Biochem.* 136:169–176. <https://doi.org/10.1093/jb/mvh108>
- Little, N.A., N.D. Hastie, and R.C. Davies. 2000. Identification of WTAP, a novel Wilms' tumour 1-associating protein. *Hum. Mol. Genet.* 9: 2231–2239. <https://doi.org/10.1093/oxfordjournals.hmg.a018914>
- Loh, K.H., P.S. Stawski, A.S. Draycott, N.D. Udeshi, E.K. Lehrman, D.K. Wilton, T. Svinkina, T.J. Deerinck, M.H. Ellisman, B. Stevens, et al. 2016. Proteomic Analysis of Unbounded Cellular Compartments: Synaptic Clefts. *Cell*. 166:1295–1307.e21. <https://doi.org/10.1016/j.cell.2016.07.041>
- Long, J.C., and J.F. Caceres. 2009. The SR protein family of splicing factors: master regulators of gene expression. *Biochem. J.* 417:15–27. <https://doi.org/10.1042/BJ20081501>
- Malinová, A., Z. Cvačková, D. Matějů, Z. Hořejší, C. Abéza, F. Vandermoere, E. Bertrand, D. Staněk, and C. Verheggen. 2017. Assembly of the U5 snRNP component PRPF8 is controlled by the HSP90/R2TP chaperones. *J. Cell Biol.* 216:1579–1596. <https://doi.org/10.1083/jcb.201701165>
- Martell, J.D., T.J. Deerinck, Y. Sancak, T.L. Poulos, V.K. Mootha, G.E. Sosinsky, M.H. Ellisman, and A.Y. Ting. 2012. Engineered ascorbate peroxidase as a genetically encoded reporter for electron microscopy. *Nat. Biotechnol.* 30:1143–1148. <https://doi.org/10.1038/nbt.2375>
- Martell, J.D., M. Yamagata, T.J. Deerinck, S. Phan, C.G. Kwa, M.H. Ellisman, J.R. Sanes, and A.Y. Ting. 2016. A split horseradish peroxidase for the detection of intercellular protein-protein interactions and sensitive visualization of synapses. *Nat. Biotechnol.* 34:774–780. <https://doi.org/10.1038/nbt.3563>
- Marzahn, M.R., S. Marada, J. Lee, A. Nourse, S. Kenrick, H. Zhao, G. Ben-Nissan, R.-M. Kolaitis, J.L. Peters, S. Pounds, et al. 2016. Higher-order oligomerization promotes localization of SPOP to liquid nuclear speckles. *EMBO J.* 35:1254–1275. <https://doi.org/10.15252/embj.201593169>
- Mellacheruvu, D., Z. Wright, A.L. Couzens, J.-P. Lambert, A.M. St-Denis, T. Li, Y.V. Miteva, S. Hauri, M.E. Sardi, T.Y. Low, et al. 2013. The CRAPome: a contaminant repository for affinity purification-mass spectrometry data. *Nat. Methods*. 10:730–736. <https://doi.org/10.1038/nmeth.2557>
- Mintz, P.J., S.D. Patterson, A.F. Neuwald, C.S. Spahr, and D.L. Spector. 1999. Purification and biochemical characterization of interchromatin granule clusters. *EMBO J.* 18:4308–4320. <https://doi.org/10.1093/emboj/18.15.4308>
- Mootha, V.K., J. Bunkenborg, J.V. Olsen, M. Hjerrild, J.R. Wisniewski, E. Stahl, M.S. Bolouri, H.N. Ray, S. Sihag, M. Kamal, et al. 2003. Integrated analysis of protein composition, tissue diversity, and gene regulation in mouse mitochondria. *Cell*. 115:629–640. [https://doi.org/10.1016/S0092-8674\(03\)00926-7](https://doi.org/10.1016/S0092-8674(03)00926-7)
- Müller-Ott, K., F. Erdel, A. Matveeva, J.P. Mallm, A. Rademacher, M. Hahn, C. Bauer, Q. Zhang, S. Kaltofen, G. Schotta, et al. 2014. Specificity, propagation, and memory of pericentric heterochromatin. *Mol. Syst. Biol.* 10: 746. <https://doi.org/10.15252/msb.20145377>
- Narita, M., M. Narita, V. Krizhanovsky, S. Nuñez, A. Chicas, S.A. Hearn, M.P. Myers, and S.W. Lowe. 2006. A novel role for high-mobility group A proteins in cellular senescence and heterochromatin formation. *Cell*. 126:503–514. <https://doi.org/10.1016/j.cell.2006.05.052>
- Obuse, C., H. Yang, N. Nozaki, S. Goto, T. Okazaki, and K. Yoda. 2004. Proteomic analysis of the centromere complex from HeLa interphase cells: UV-damaged DNA binding protein 1 (DDB-1) is a component of the CEN-complex, while BMI-1 is transiently co-localized with the centromeric region in interphase. *Genes Cells*. 9:105–120. <https://doi.org/10.1111/j.1365-2443.2004.00705.x>
- Onyango, D.O., S.M. Howard, K. Neherin, D.A. Yanez, and J.M. Stark. 2016. Tetratricopeptide repeat factor XAB2 mediates the end resection step of homologous recombination. *Nucleic Acids Res.* 44:5702–5716. <https://doi.org/10.1093/nar/gkw275>
- Patel, A., H.O. Lee, L. Jawerth, S. Maharana, M. Jahnel, M.Y. Hein, S. Stoynov, J. Mahamid, S. Saha, T.M. Franzmann, et al. 2015. A Liquid-to-Solid Phase Transition of the ALS Protein FUS Accelerated by Disease Mutation. *Cell*. 162:1066–1077. <https://doi.org/10.1016/j.cell.2015.07.047>
- Phair, R.D., and T. Misteli. 2000. High mobility of proteins in the mammalian cell nucleus. *Nature*. 404:604–609. <https://doi.org/10.1038/35007077>
- Platt, C., M. Calimano, J. Nemet, J. Bubenik, and A. Cochrane. 2015. Differential Effects of Tra2 $\beta$  Isoforms on HIV-1 RNA Processing and Expression. *PLoS One*. 10. e0125315. <https://doi.org/10.1371/journal.pone.0125315>
- Prasanth, K.V., P.A. Sacco-Bubulya, S.G. Prasanth, D.L. Spector, and J. Gall. 2003. Sequential entry of components of the gene expression machinery into daughter nuclei. *Mol. Biol. Cell*. 14:1043–1057. <https://doi.org/10.1091/mbc.e02-10-0669>
- Rai, A.K., J.X. Chen, M. Selbach, and L. Pelkmans. 2018. Kinase-controlled phase transition of membraneless organelles in mitosis. *Nature*. 559: 211–216. <https://doi.org/10.1038/s41586-018-0279-8>
- Rhee, H.-W., P. Zou, N.D. Udeshi, J.D. Martell, V.K. Mootha, S.A. Carr, and A.Y. Ting. 2013. Proteomic mapping of mitochondria in living cells via spatially restricted enzymatic tagging. *Science*. 339:1328–1331. <https://doi.org/10.1126/science.1230593>
- Roux, K.J., D.I. Kim, M. Raida, and B. Burke. 2012. A promiscuous biotin ligase fusion protein identifies proximal and interacting proteins in mammalian cells. *J. Cell Biol.* 196:801–810. <https://doi.org/10.1083/jcb.201112098>
- Saitoh, N., C.S. Spahr, S.D. Patterson, P. Bubulya, A.F. Neuwald, and D.L. Spector. 2004. Proteomic analysis of interchromatin granule clusters. *Mol. Biol. Cell*. 15:3876–3890. <https://doi.org/10.1091/mbc.e04-03-0253>
- Salas-Armenteros, I., S.I. Barroso, A.G. Rondón, M. Pérez, E. Andújar, R. Luna, and A. Aguilera. 2019. Depletion of the MFAPI/SPP381 Splicing Factor Causes R-Loop-Independent Genome Instability. *Cell Rep.* 28:1551–1563.e1557.
- Sasaki-Osugi, K., C. Imoto, T. Takahara, H. Shibata, and M. Maki. 2013. Nuclear ALG-2 protein interacts with Ca<sup>2+</sup> homeostasis endoplasmic reticulum protein (CHERP) Ca<sup>2+</sup>-dependently and participates in regulation of alternative splicing of inositol trisphosphate receptor type 1 (IP3R1) pre-mRNA. *J. Biol. Chem.* 288:33361–33375. <https://doi.org/10.1074/jbc.M113.497479>
- Sharma, A., H. Takata, K. Shibahara, A. Bubulya, and P.A. Bubulya. 2010. Son is essential for nuclear speckle organization and cell cycle progression. *Mol. Biol. Cell*. 21:650–663. <https://doi.org/10.1091/mbc.e09-02-0126>
- Shevtsov, S.P., and M. Dundr. 2011. Nucleation of nuclear bodies by RNA. *Nat. Cell Biol.* 13:167–173. <https://doi.org/10.1038/ncb2157>
- Singh, K.K., S. Erkelenz, S. Rattay, A.K. Dehof, A. Hildebrandt, K. Schulze-Osthoff, H. Schaal, and C. Schwer. 2010. Human SAP18 mediates assembly of a splicing regulatory multiprotein complex via its ubiquitin-like fold. *RNA*. 16:2442–2454. <https://doi.org/10.1261/rna.2304410>
- Solomon, S., Y. Xu, B. Wang, M.D. David, P. Schubert, D. Kennedy, and J.W. Schrader. 2007. Distinct structural features of caprin-1 mediate its interaction with G3BP-1 and its induction of phosphorylation of eukaryotic translation initiation factor 2 $\alpha$ , entry to cytoplasmic stress granules, and selective interaction with a subset of mRNAs. *Mol. Cell Biol.* 27:2324–2342. <https://doi.org/10.1128/MCB.02300-06>
- Spector, D.L., and H.C. Smith. 1986. Redistribution of U-snRNPs during mitosis. *Exp. Cell Res.* 163:87–94. [https://doi.org/10.1016/0014-4827\(86\)90560-4](https://doi.org/10.1016/0014-4827(86)90560-4)
- Taylor, S.W., E. Fahy, B. Zhang, G.M. Glenn, D.E. Warnock, S. Wiley, A.N. Murphy, S.P. Gaucher, R.A. Capaldi, B.W. Gibson, et al. 2003. Characterization of the human heart mitochondrial proteome. *Nat. Biotechnol.* 21:281–286. <https://doi.org/10.1038/nbt793>
- Terada, Y., and Y. Yasuda. 2006. Human minodeficiency virus type 1 Vpr induces G2 checkpoint activation by interacting with the splicing factor SAPI45. *Mol. Cell Biol.* 26:8149–8158. <https://doi.org/10.1128/MCB.01170-06>
- Teves, S.S., L. An, A.S. Hansen, L. Xie, X. Darzacq, and R. Tjian. 2016. A dynamic mode of mitotic bookmarking by transcription factors. *eLife*. 5. e22280. <https://doi.org/10.7554/eLife.22280>

- Thul, P.J., L. Åkesson, M. Wiking, D. Mahdessian, A. Geladaki, H. Ait Blal, T. Alm, A. Asplund, L. Björk, L.M. Breckels, et al. 2017. A subcellular map of the human proteome. *Science*. 356:eaal3321.
- Trembley, J.H., S. Tatsumi, E. Sakashita, P. Loyer, C.A. Slaughter, H. Suzuki, H. Endo, V.J. Kidd, and A. Mayeda. 2005. Activation of pre-mRNA splicing by human RNPS1 is regulated by CK2 phosphorylation. *Mol. Cell. Biol.* 25: 1446–1457. <https://doi.org/10.1128/MCB.25.4.1446-1457.2005>
- Ulrich, A.K.C., M. Seeger, T. Schütze, N. Bartlick, and M.C. Wahl. 2016. Scaffolding in the Spliceosome via Single  $\alpha$  Helices. *Structure*. 24: 1972–1983. <https://doi.org/10.1016/j.str.2016.09.007>
- Umehara, H., Y. Nishii, M. Morishima, Y. Kakehi, N. Kioka, T. Amachi, J. Koizumi, M. Hagiwara, and K. Ueda. 2003. Effect of cisplatin treatment on speckled distribution of a serine/arginine-rich nuclear protein CROP/Luc7A. *Biochem. Biophys. Res. Commun.* 301:324–329. [https://doi.org/10.1016/S0006-291X\(02\)03017-6](https://doi.org/10.1016/S0006-291X(02)03017-6)
- van Gijlswijk, R.P., J. Wiegant, A.K. Raap, and H.J. Tanke. 1996. Improved localization of fluorescent tyramides for fluorescence in situ hybridization using dextran sulfate and polyvinyl alcohol. *J. Histochem. Cytochem.* 44:389–392. <https://doi.org/10.1177/44.4.8601698>
- van Gijlswijk, R.P., H.J.M.A.A. Zijlmans, J. Wiegant, M.N. Bobrow, T.J. Erickson, K.E. Adler, H.J. Tanke, and A.K. Raap. 1997. Fluorochrome-labeled tyramides: use in immunocytochemistry and fluorescence in situ hybridization. *J. Histochem. Cytochem.* 45:375–382. <https://doi.org/10.1177/002215549704500305>
- Verdaasdonk, J.S., and K. Bloom. 2011. Centromeres: unique chromatin structures that drive chromosome segregation. *Nat. Rev. Mol. Cell Biol.* 12:320–332. <https://doi.org/10.1038/nrm3107>
- Wang, G., C.L. Achim, R.L. Hamilton, C.A. Wiley, and V. Soontornniyomkij. 1999. Tyramide signal amplification method in multiple-label immunofluorescence confocal microscopy. *Methods*. 18:459–464. <https://doi.org/10.1006/meth.1999.0813>
- Will, C.L., H. Urlaub, T. Achsel, M. Gentzel, M. Wilm, and R. Lührmann. 2002. Characterization of novel SF3b and 17S U2 snRNP proteins, including a human Prp5p homologue and an SF3b DEAD-box protein. *EMBO J.* 21: 4978–4988. <https://doi.org/10.1093/emboj/cdf480>
- Wu, J.Y., and T. Maniatis. 1993. Specific interactions between proteins implicated in splice site selection and regulated alternative splicing. *Cell*. 75:1061–1070. [https://doi.org/10.1016/0092-8674\(93\)90316-1](https://doi.org/10.1016/0092-8674(93)90316-1)
- Yamada, T., W. Fischle, T. Sugiyama, C.D. Allis, and S.I.S. Grewal. 2005. The nucleation and maintenance of heterochromatin by a histone deacetylase in fission yeast. *Mol. Cell*. 20:173–185. <https://doi.org/10.1016/j.molcel.2005.10.002>
- Yamagishi, Y., T. Honda, Y. Tanno, and Y. Watanabe. 2010. Two histone marks establish the inner centromere and chromosome bi-orientation. *Science*. 330:239–243. <https://doi.org/10.1126/science.1194498>
- Zhang, C., D.R. Dowd, A. Staal, C. Gu, J.B. Lian, A.J. van Wijnen, G.S. Stein, and P.N. MacDonald. 2003. Nuclear coactivator-62 kDa/Ski-interacting protein is a nuclear matrix-associated coactivator that may couple vitamin D receptor-mediated transcription and RNA splicing. *J. Biol. Chem.* 278:35325–35336. <https://doi.org/10.1074/jbc.M305191200>
- Zhou, A., A.C. Ou, A. Cho, E.J. Benz, Jr., and S.C. Huang. 2008. Novel splicing factor RBM25 modulates Bcl-x pre-mRNA 5' splice site selection. *Mol. Cell. Biol.* 28:5924–5936. <https://doi.org/10.1128/MCB.00560-08>

## Supplemental material

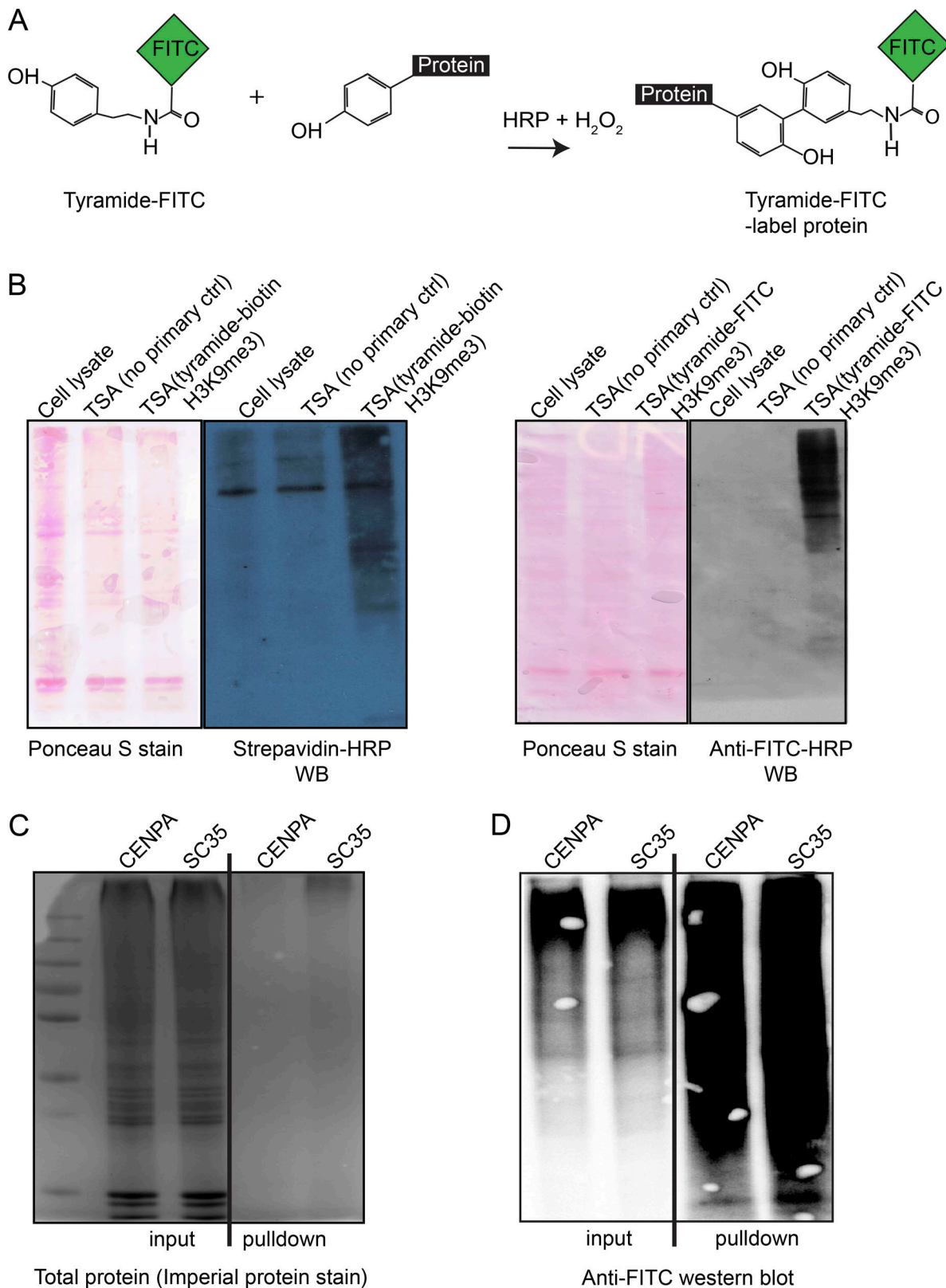


Figure S1. **TSA labeling of proteins.** (A) Chemical structure of tyramide-FITC and the labeling of proteins. (B) Western blot (WB) after TSA labeling with either tyramide-biotin or tyramide-FITC. Cell lysate without TSA reaction and a TSA reaction without primary antibody were included as controls. (C) Gel picture showing total protein staining of 0.5% of the input lysate after TSA reaction compared with 50% of the total proteins pulled down. (D) Western blot comparing FITC-labeled proteins as in C.

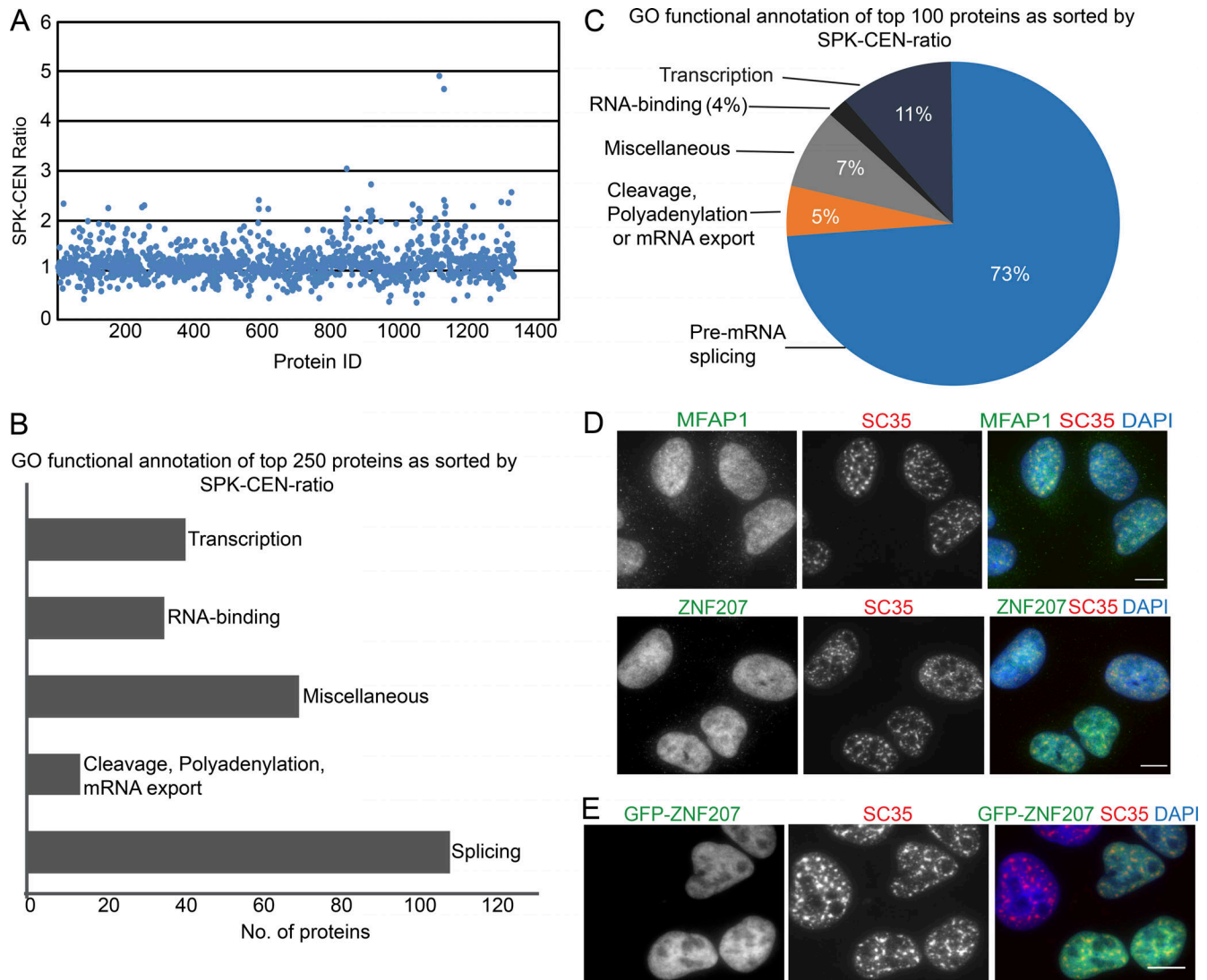


Figure S2. **Data analysis, functional annotation, and validation of potential nuclear speckle proteins.** (A) Scatter plot of the nuclear speckle versus centromere ratio (SPK-CEN ratio) of proteins. (B) Bar chart showing the GO annotated biological processes of the top 250 proteins as sorted by the SPK-CEN-Ratio. (C) Pie chart showing the GO annotated biological processes of the top 100 proteins as sorted by the SPK-CEN ratio. (D) Immunofluorescence of U2OS cells costained with anti-MFAP1 or anti-ZNF207 (green) and SC35 (red) after PFA fixation. (E) Anti-SC35 immunostaining (red) of U2OS cells expressing GFP-ZNF207 (green) and fixed with PFA shows loss of GFP-ZNF207 fluorescence after fixation. Scale bars: 10  $\mu$ m.

Downloaded from https://rpress.org/jcb/article-pdf/219/9/e201910207/1046779/jcb\_201910207.pdf by California Institute Of Technology user on 01 July 2020

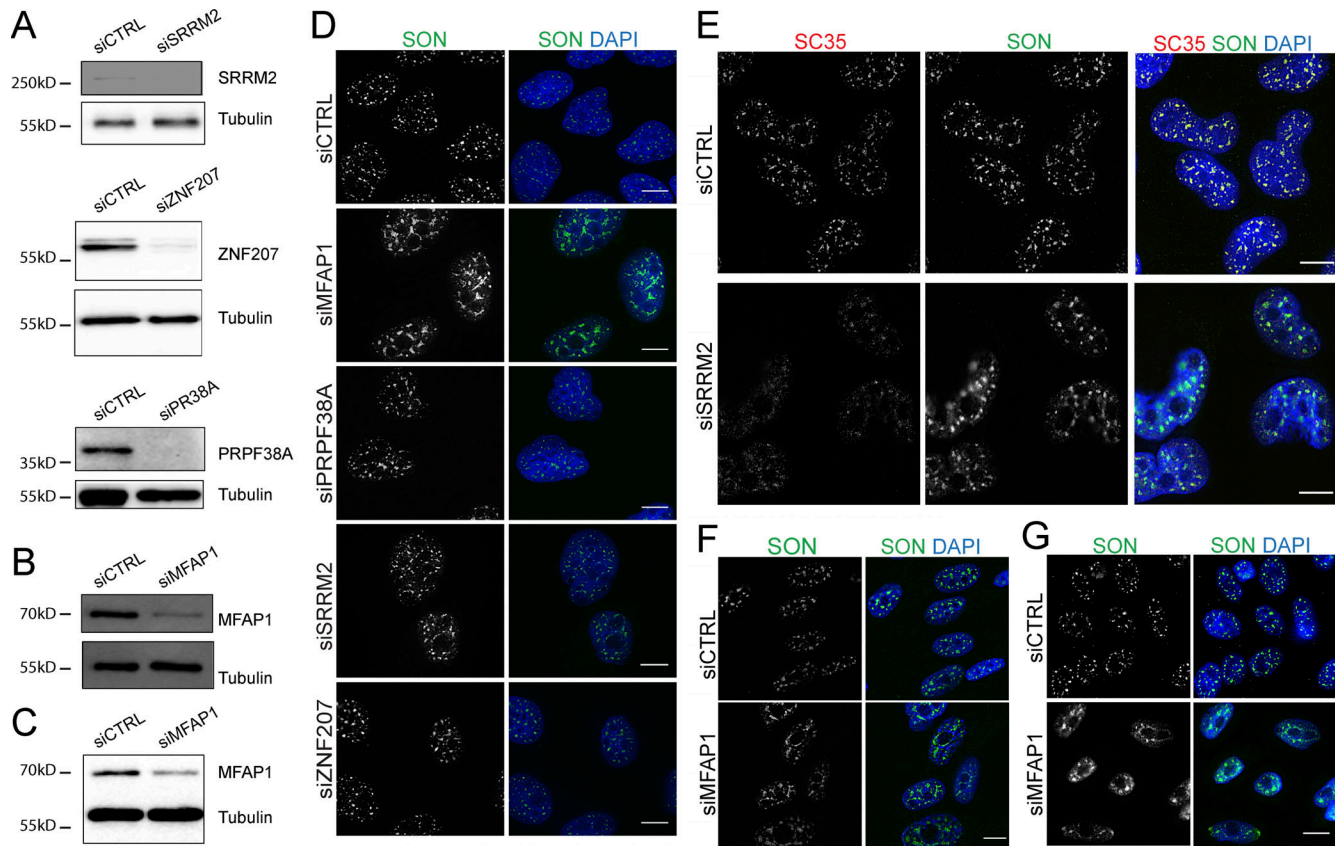


Figure S3. **MFAP1 KD specifically increases nuclear speckle size.** (A) Western blots showing RNAi depletion of the indicated proteins (SRRM2, ZNF207, or PRPF38A) in U2OS cells. (B and C) Western blot showing the depletion of MFAP1 in TIG3 (B) or CHO (C) cells. Tubulin was detected as loading control. (D) Representative anti-SON immunofluorescence images of U2OS cells following siRNA treatment as indicated. (E) Representative anti-SON and anti-SC35 coimmunostaining of U2OS cells transfected with control siRNA (siCTRL) or siRNA against SRRM2 (siSRRM2). (F and G) Anti-SON immunofluorescence images of TIG3 cells (F) or CHO cells (G) after transfection with control siRNA (siCTRL) or siRNA against MFAP1 (siMFAP1). DNA (blue) was stained with DAPI. Scale bars: 10  $\mu$ m.

Downloaded from https://rpress.org/jcb/article-pdf/219/9/e201910207/1046779/jcb\_201910207.pdf by California Institute Of Technology user on 01 July 2020

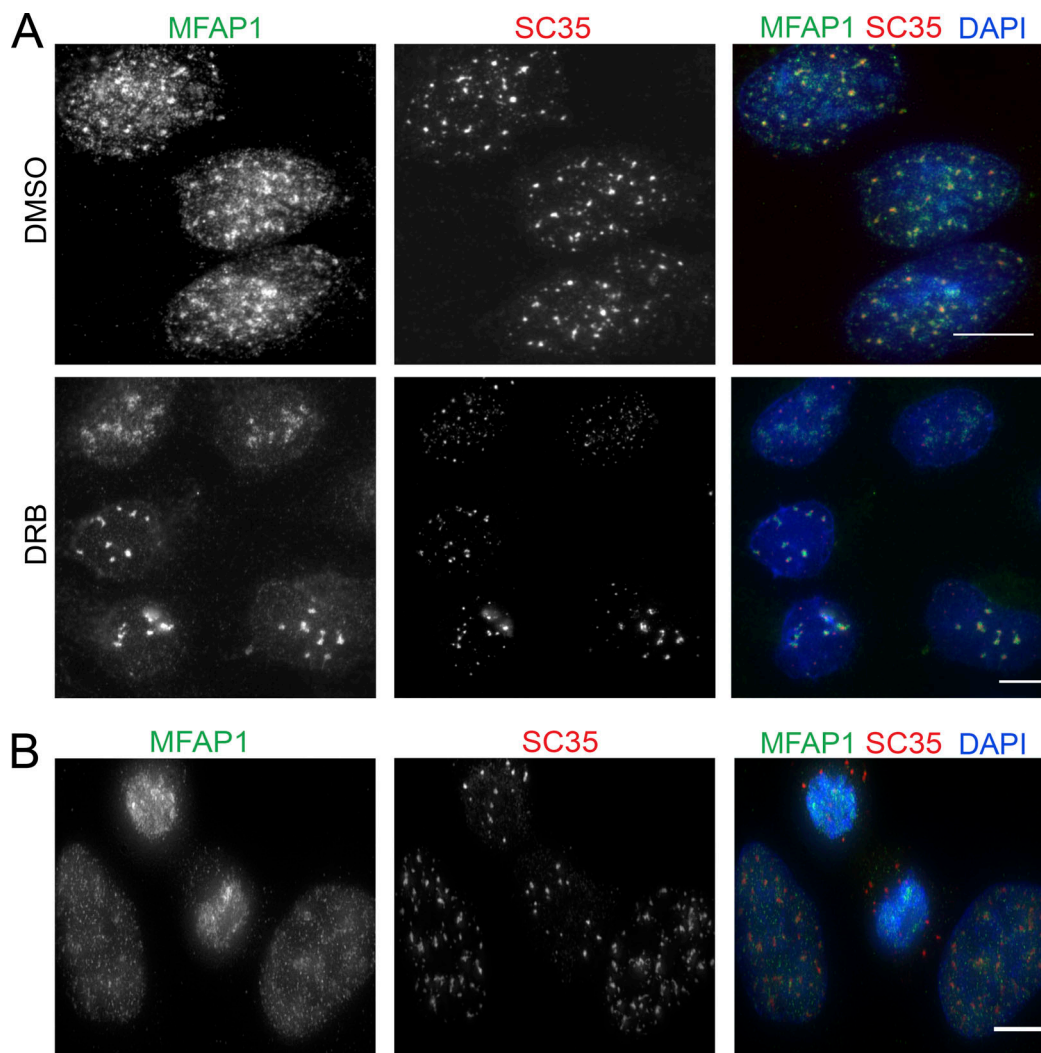


Figure S4. **Nuclear speckle localization of MFAP1.** (A) Immunofluorescence images of U2OS cells after SC35 and MFAP1 coimmunostaining following treatment with either DMSO or DRB for 2 h. Cells were fixed with 100% methanol. (B) Representative immunofluorescence image of a mitotic U2OS cell after SC35 and MFAP1 coimmunostaining following PFA fixation. DNA (blue) was stained with DAPI. Scale bars: 10  $\mu$ m.

Video 1. **Nuclear speckles in MFAP1-depleted cells relocate to nucleolar periphery after DRB treatment.** Time-lapse video of MFAP1-depleted U2OS cell expressing GFP-ZNF207 nuclear speckle marker and treated with DRB. Arrow points to a nuclear speckle that moves to and then merges with nucleolar periphery. After contacting the nucleolar periphery, the speckle flattens in shape and its contents appear to then spread out and partially encircle the nucleolar periphery. Time (top left corner) in hours:minutes format.

Video 2. **GFP-MFAP1 segregates into foci adjacent to nuclear speckles after DRB treatment.** Time-lapse video of a U2OS cell coexpressing GFP-MFAP1 (green) and mCherry-SON (red) and treated with DRB. Time-lapse image acquisition started  $\sim$ 15 min after DRB treatment. Arrowheads indicate GFP-MFAP1 foci next to nuclear speckles (red). Numbers at the top left are time points in hours:minutes format.

Video 3. **Reversal of RNA pol II transcription inhibition results in disappearance of MFAP1-positive droplet-like foci adjacent to nuclear speckles.** Time-lapse video of a U2OS cell coexpressing GFP-MFAP1 (green) and mCherry-SON (red). Cells were treated for 2 h with DRB to induce MFAP1 foci and then rinsed with complete growth media before imaging. Arrowheads indicate GFP-MFAP1 foci adjacent to nuclear speckles that partially disappear as GFP-MFAP1 reenters nuclear speckles. Time (top left) in hours:minutes format.

Video 4. **Reversal of RNA pol II transcription inhibition results in disappearance of GFP-PRPF38A droplet-like foci adjacent to nuclear speckles.** Time-lapse video of a U2OS cell coexpressing GFP-PRPF38A (green) and mCherry-SON (red). Cells were treated for 2 h with DRB to induce GFP-PRPF38A foci and then rinsed with complete growth media before imaging. Arrowheads indicate GFP-PRPF38A foci that disappear as GFP-PRPF38A reenters nuclear speckles. Time (top left) in hours:minutes format.

Video 5. **GFP-MFAP1 reenters nucleus and forms droplet-like foci before reentry of SON protein and nuclear speckle reassembly after mitosis.** Time-lapse video of a mitotic U2OS cell expressing GFP-MFAP1 (green) and mCherry-SON (red). Time points (top left corner) in hours:minutes format.

Video 6. **GFP-MFAP1 localizes and accumulates into foci in the nucleus before complete chromatin decondensation.** Time-lapse video of a mitotic U2OS cell expressing GFP-MFAP1 (green). Arrowheads indicate GFP-MFAP1-positive foci. Numbers at top left are time points in the hours:minutes format. DNA (red) was visualized with SiR-Hoechst.

**Table S1 is provided online and shows MS data.**